

UWL REPOSITORY
repository.uwl.ac.uk

Performance analysis and design implementation of a novel polymer hollow fiber liquid desiccant dehumidifier with aqueous potassium formate

Chen, Xiangjie, Zhang, Nan, Su, Yuehong, Aydin, Devrim, Zheng, Hongfei, Bai, Hongyu, Georgakis, Apostolos, Jarimi, Hasila and Riffat, Saffa (2019) Performance analysis and design implementation of a novel polymer hollow fiber liquid desiccant dehumidifier with aqueous potassium formate. *Thermal Science and Engineering Progress*, 13. p. 100366.

<http://dx.doi.org/10.1016/j.tsep.2019.100366>

This is the Accepted Version of the final output.

UWL repository link: <https://repository.uwl.ac.uk/id/eprint/6331/>

Alternative formats: If you require this document in an alternative format, please contact: open.research@uwl.ac.uk

Copyright: Creative Commons: Attribution-Noncommercial-No Derivative Works 4.0

Copyright and moral rights for the publications made accessible in the public portal are retained by the authors and/or other copyright owners and it is a condition of accessing publications that users recognise and abide by the legal requirements associated with these rights.

Take down policy: If you believe that this document breaches copyright, please contact us at open.research@uwl.ac.uk providing details, and we will remove access to the work immediately and investigate your claim.

Performance analysis and design implementation of a novel polymer hollow fiber liquid desiccant dehumidifier with aqueous potassium formate

Nan Zhang¹, Xiangjie Chen^{2,3}, Yuehong Su², Devrim Aydin⁴, Hongfei Zheng^{1,*}, Hongyu Bai², Apostolos Georgakis⁵, Hasila Jarimi², Saffa Riffat²

¹School of Mechanical Engineering, Beijing Institute of Technology, Beijing 100081, China

²Department of Architecture and Built Environment, the University of Nottingham, University Park, Nottingham, NG7 2RD, UK.

³Department of Energy and Power Engineering, University of Shanghai for Science and Technology, Jungong Road No. 516, Shanghai, 200031, China

⁴Department of Mechanical Engineering, Eastern Mediterranean University, G. Magosa, TRNC Mersin 10, Turkey.

⁵School of Computing and Engineering, University of West London, W5 5RF, UK.

Contact: Xiangjie Chen; Email:xiangjie.chen@nottingham.ac.uk ; Hongfei Zheng;

Email:hongfeizh@bit.edu.cn

Abstract

A novel cross-flow liquid desiccant polymer hollow fiber dehumidifier (PHFD) is investigated numerically in this paper.

The main objective of this research is to simulate, validate the numerical model for future design implementations. The experimental verified simulation data will be used to develop a set of design and implementation tables and charts as the guidance for selecting the number of fibres and the solution-to-air mass flow ratio of the PHDF under given conditions. A numerical model is developed to simulate the performance of the proposed innovative dehumidifier. This model is validated against three sets of data, i.e, the experimental obtained testing results, analytical correlations and the modelling results from the literature. The influence of various operating conditions such as inlet air properties (i.e. velocity, relative humidity) and inlet solution properties (i.e. temperature, concentration, mass flow rate) on the dehumidification sensible, latent, and total effectiveness, moisture removal rate are numerically analyzed. Dimensionless parameters including the number of heat transfer unit (NTU) and the number of mass transfer unit (NTU_m), the solution to air mass flow rate ratio (m^*), and the air to solution specific humidity ratio (ω_r^*) have been used to evaluate the system performance. The results show that the increase in NTU and NTU_m lead to a substantial change in dehumidification effectiveness. When the NTU increases from 0.47 to 7, the sensible effectiveness rises from 0.35 to 0.95. Increasing ω_r^* is another good option for increasing the amount of the absorbed moisture without influencing the latent effectiveness. For an increase of ω_r^* from 1.4 to 2.2, the air inlet and outlet specific humidity difference varies in the range of 0.008 kg/kg and 0.018 kg/kg.

Keywords: Polymer hollow fibre dehumidifier, potassium formate solutions, heat transfer, mass transfer, numerical analysis, experimental validation, performance implementation

43 **1. Introduction**

44 Around 40% and 50% of the EU's total energy and electricity consumption, respectively, takes
45 place in buildings [1]. The majority of this comes from the combustion of fossil fuels,
46 contributing to approximate 36% of the EU's total carbon emissions [2]. By 2025, the installed
47 air-conditioning capacity in Europe is predicted to further increase by 50%-60% compared with
48 that in 2010 [3]. The above situation has fueled research into energy-efficient and
49 environmentally-friendly air-conditioning systems.

50 Dehumidification is an inseparable part of air conditioning, both for commercial and residential
51 cooling, and for humidity control in a wide range of industries (e.g. food, textile, wood
52 processing, printing, and crop drying). Recent research into efficient dehumidifiers has been
53 growingly focusing on liquid desiccant-integrated processes [4], and evaporative cooling [5, 6].
54 This approach introduces important advantages compared with the conventional vapour
55 compression (VC) systems. Firstly, it does not require refrigerants such as CFCs and HFCs,
56 which are known to be detrimental to ozone depletion and global warming. Secondly, it results
57 in energy savings of around 30% [5] by avoiding the deep-cooling-and-reheating cycles (VC
58 systems remove moisture from the air by cooling it below its dew point so that water vapour
59 condenses on a cooling coil, and then reheat the dehumidified air to reach the desired
60 temperature). Liquid desiccant-based systems dehumidify the air by utilizing the natural
61 hygroscopic properties of desiccant materials, i.e. their ability to absorb moisture. Finally,
62 thanks to their lower consumption, liquid desiccant dehumidifiers can easily be powered by
63 renewable energy (e.g. solar, wind) [7-10], further reducing carbon emissions.

64 Central to the design of liquid desiccant dehumidifiers is the flow pattern in which the incoming
65 humid air gets in contact with the moisture absorbing material. There are two broad types of
66 dehumidifier designs: direct contact [11-17] and indirect contact [18-21]. Direct contact simply
67 exposes the liquid desiccant to the flowing air. A two stage liquid desiccant dehumidifier
68 proposed by Xiong et al. [22] showed a double fold thermal performance improvement
69 compared with a conventional dehumidifier. A fin-tube type internally-cooled liquid desiccant
70 dehumidifier was explored by Luo et al. using experimental analysis [23] and CFD modeling
71 [24]. Ou et al. [25], conducted experimental and analytical studies on a combined system with
72 a cooling coil, obtaining 22.3% of energy savings.

73 A disadvantage of direct contact is that the air passing over the liquid desiccant results in
74 droplets of the desiccant migrating across the dehumidifier. To mitigate this, thin membrane
75 plate dehumidifiers with different configurations have been studied by various researchers. A
76 cross flow membrane contactor was analyzed by Das and Jain [26] using LiCl as the liquid
77 desiccant. The results indicated that the reduced air channel gap within the membrane contactor
78 lead to improved energy efficiency. Ge et al. [27-30] presented a counter-cross-flow single-
79 plate membrane contactor with an air gap of 5mm using again LiCl as the desiccant. Their
80 numerical and experimental results confirmed that the solution concentration and the moisture
81 flow rate were the main factors for efficient moisture removal. Moghaddam et al. [31-34] tested
82 an air-to-liquid membrane energy exchanger using LiCl. The results showed that the
83 dehumidifier effectiveness (both sensible and latent) was sensitive to the concentration of the
84 inlet solution.

85 Despite the extensive research on the performance of various packed beds [16, 17, 22, 25] or
86 thin membrane plate dehumidifiers [27, 31], the liquid droplet carryover problem could not be
87 solved. Since most liquid desiccants (LiCl, CaCl₂ and LiBr) are corrosive and harmful to health,
88 the spreading, as well as the proper subsequent removal of their carryovers becomes a major
89 problem. In order to address this, permeable polymer hollow fiber dehumidifiers (PHFD) have
90 been proposed as an alternative for direct contact dehumidifiers. Due to the microscopic size of
91 its pore (less than 100µm) [35], the hollow fibre allows the moisture of the incoming air to
92 penetrate through its porous wall, while preventing any liquid desiccant droplets from getting
93 in contact with the processed air. Moreover, the small inside diameter (less than 0.1mm) of the
94 polymer hollow fiber leads to significantly enhanced surface contact areas, which can be
95 regarded as another great advantage of the PHFD. A numerical simulation model for a hollow-
96 fiber dehumidification system was proposed by Zhang et al. [36]. They concluded that the
97 dehumidifier's effectiveness and dimensionless parameters were influenced by the varying air
98 flow rate. Huang et al. [37] analyzed the coupled heat and mass transfer in parallel-plate
99 membranes by numerical analysis. Their findings showed that the boundary conditions were
100 non-uniform both in the air side and the solution side. A CFD package-FLUENT module was
101 set-up by Zhang et al. [38]. Their analytical data indicated that the packing ratio had a major
102 impact on the flow distribution. The above team, has recently also worked on integrating liquid
103 desiccant-based membranes into heat pumps [39, 40] and heat recovery systems [41].

104

105 The research work presented in this paper aims to bridge the following research gaps: (1) As
106 summarized in Table 1, the work published in the field of hollow fiber integrated
107 dehumidification systems has mostly focused on theoretical modelling [36-39], with hardly any
108 experimental results. Attempts have been made to obtain the overall heat and mass transfer
109 coefficients for a polymer hollow fiber integrated shell-and-tube heat exchanger [42]. Due to
110 the difficulties in the manufacturing process of PHFD (especially related to potting the hollow
111 fiber bundles), very limited effort has been made to validate the models against experimental
112 testing results. (2) The dehumidification capacity of PHFD with aqueous potassium formate
113 (KCOOH) as the liquid desiccant has not been adequately addressed in the literature. With its
114 advantages of low price, low toxicity and low corrosiveness compared with other liquid
115 desiccants [43], the aqueous potassium formate solution is a preferable, environmentally
116 friendly liquid desiccant. The associated higher vapour pressure of KCOOH solutions means
117 that smaller amounts of energy are required for the regeneration stage [43], leading to a great
118 energy saving potential for the proposed PHFD. (3) Most importantly, previous modelling
119 works presented in the literature are largely based on specific working conditions and certain
120 PHFD module configurations, which can hardly be duplicated practically in the design of PHFD
121 modules for arbitrarily given operating conditions. (4) The effects of different fiber numbers on
122 the dehumidification performance of PHFD have not been investigated to date. A detailed
123 summary of previous research work and the research gap this paper is aiming to bridge is shown
124 in Table 1.

125 This paper introduces numerical and experimental investigations of a polymer hollow fiber
126 integrated dehumidifier (PHFD) with a potassium formate solution. It starts with numerical
127 evaluations of heat and mass transfer in such cross-flow liquid desiccant PHFDs. As opposed
128 to thin plate membrane contactors [31-34], the developed model takes into consideration the

129 porous and permeable feature of the polymer hollow fibers. Firstly, the derived mathematical
 130 model was verified against three sets of data, i.e. experimental testing results, analytical results,
 131 and published simulation results. Then, the impact of various operating conditions, i.e. the inlet
 132 air properties (velocity, relative humidity), and the inlet solution properties (concentration, mass
 133 flow rate, temperature) on: (a) the dehumidification effectiveness (sensible, latent, and total),
 134 (b) the moisture removal rate, and (c) the outlet parameters (air temperature and specific
 135 humidity), were numerically calculated and analyzed using the verified model. Dimensionless
 136 parameters including the number of heat transfer unit (NTU) and number of mass transfer unit
 137 (NTU_m), the solution-to-air mass flow ratio (m^*), the air-to-solution specific humidity ratio
 138 (ω_r^*) have been employed to evaluate the dehumidification performance of the proposed PHFD.
 139 Finally, the effects of fiber number on the dehumidification performance have been analyzed.
 140 Based on the numerical modelling, a set of PHFD performance tables and charts have been
 141 developed and verified against experimental results [44]. These can serve as a guidance for the
 142 selection of appropriate number of fibres and the solution-to-air mass flow ratio of the PHDFs
 143 under given conditions. With no iterative calculation required, this would give the designers
 144 great convenience. The outcomes in the form of tables and charts can be used in the design of
 145 aqueous KCOOH based PHFD. The research approach in this paper can also be adopted for
 146 other types of liquid desiccants and PHFD configurations.

147 Table 1 Summary of the existing works and the research gap bridged by the present research

Reference	Dehumidifier type	Flow patter	Direct/indirect contact between air and liquid desiccant	Numerical/ Experimental investigation	Desiccant solution	Research methodology and conclusion
Peng and Zhang [7]	Packed bed	Parallel flow	Direct	Numerical	LiCl	The analytical results were proved to agree well with modelling data.
Li et al. [8]	Packed bed	Parallel flow	Direct	Both	LiCl	The proposed simplified model agreed well with the experimental data.
Xiao et al. [9]	Packed bed	Counter flow	Direct	Numerical	LiCl	The proposed outdoor air liquid desiccant system could be adopted for humid and hot climates, with the system performance improvement of 19.9-38.4%.
Wang et al. [16]	Packed bed	Parallel flow	Direct	Both	LiCl	The work conducted was mainly focused on the input and output data for system control and optimization, therefore no iterative process was involved.
Wu et al. [17]	Packed bed	Counter flow	Direct	Numerical	LiCl	The control strategy applied in this work avoids the continuous solution exchange, which allowed a series of dehumidifiers to work together for large scale building applications.

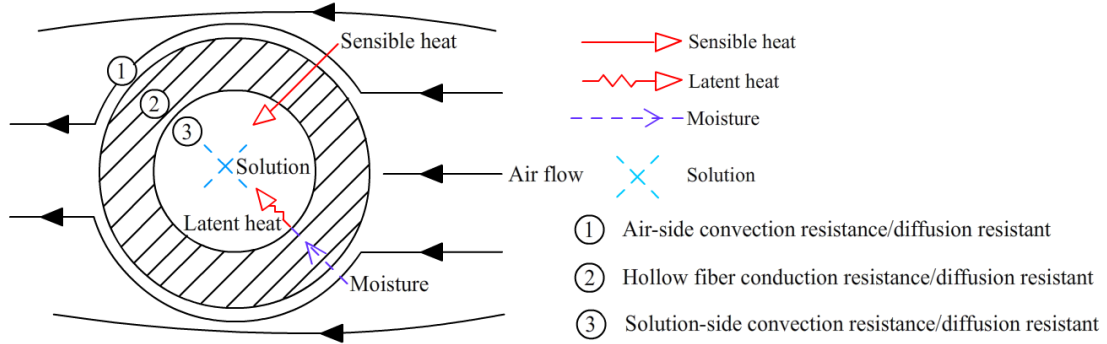
Xiong et al. [22]	Packed bed	Counter flow	Direct	Numerical	CaCl ₂	The two-stage dehumidification system was shown to offer significant performance improvement, with thermal COP of 0.73 and exergy efficiency of 23%.
Luo et al. [23, 24]	Fin tube heat exchanger	Counter flow	Indirect	Both	LiCl	The proposed fin type dehumidifier was made of light weight, corrosion resistant metal, which proved to offer dehumidification efficiency above 60%.
Moghaddam et al. [31]	Thin plate membrane energy exchanger	Counter-cross flow	Indirect	Both	LiCl	Made from semi-permeable membrane panels, the dehumidifier was designed with 2.4mm solution channel sandwiched between two solution panels.
Zhang et al. [36] and Huang et al. [37]	Polymer hollow fiber membrane contactor	Cross flow	Indirect	Numerical	LiCl	A free surface model with defined boundary conditions was developed to evaluate hollow fiber membrane module. However, the experimental results were not available.
Zhang et al. [39, 40]	Two stage hollow fiber membrane contactor	Counter flow	Indirect	Numerical	LiCl	A heat pump powered two-stage dehumidification system using membrane as the dehumidifier was numerically analyzed with performance improvement of 20% against single stage system. However, the model was not validated against experimental results.
The present work	Polymer hollow fiber integrated dehumidifier (PHFD)	Cross flow	Indirect	Both	KCOOH (Potassium formate)	Model validation have been carried out in three parts: validation against 1) laboratory obtained testing results, 2) previous established analytical results and 3) other published simulation results from the literature. Based on this, a set of PHFD performance tables and charts have been developed, which will be easily applied by designers in the practical cases.

148 2. The mathematical model

149 2.1 Heat/mass transfer coefficients for air side and solution side

150 As shown in Fig. 1, the PHFD module is designed as the interface between air flow and
151 solution flow, which respectively occur outside and inside of the hollow fibers. The heat
152 and mass transfer process of the PHFD model can be considered as three mechanisms: the
153 sensible and latent heat transfer between the air side and the solution side, and the moisture
154 transfer from the air side into the solution side. Therefore, the heat and mass transfer
155 coefficients for both the air side and solution side can be calculated using the modified

156 Gnielinski correlation [45, 46] and the Leveque equation [47, 48], as described in the
 157 following sections.



158

159 Fig. 1 Heat and mass transfer scheme of the PHFD model

160 2.1.1 Solution-side heat and mass transfer coefficient

161 The heat transfer coefficient h (W/m²K) at the solution side can be determined by the Nusselt
 162 number, which can be calculated by the following Gnielinski correlation [45, 46] with $\frac{RePrd_i}{L} <$
 163 100:

164
$$Nu_{sol} = Nu_{lim} + \frac{0.085 \left[\frac{RePrd_i}{L} \right]}{1 + 0.047 \left[\frac{RePrd_i}{L} \right]^{0.67}} \left(\frac{v_b}{v_s} \right)^{0.14}$$
 (1)

166 Where the subscripts 'b' and 's' refer to bulk and surface respectively. For the laminar flow
 167 inside the hollow fiber, the lower limit value of the Nusselt number (Nu_{lim}) is 3.658[45]. The
 168 relationship between Nusselt number and the heat transfer coefficient can be expressed as:

169
$$Nu_{sol} = \frac{hd_i}{\lambda}$$
 (2)

171 Where d_i (m) is the fiber inside diameter, and λ (W/mK) is the thermal conductivity.

172 The mass transfer coefficient k (m/s) is related to the Sherwood number, which can be defined
 173 as:

174
$$Sh_{sol} = \frac{kd_i}{\psi_w}$$
 (3)

176 The Sherwood number can be derived from the Leveque equation[47, 48] which is suitable for
 177 tube laminar flows ($Re < 2300$) with small fiber inside diameter ($d_i < 1.5mm$) and Graetz
 178 Number ($Gz = \frac{ud_i}{\psi_w L}$) over 25.

179
$$Sh_{sol} = 1.62 \left(\frac{d_i^2 u_{sol,i}^2}{L \psi_w} \right)^{\frac{1}{3}}$$
 (4)

180

181 Where ψ_w (m²/s) represents water diffusivity in the solution inside the hollow fiber, d_i (m) is
 182 the fiber inside diameter, $u_{sol,i}$ (m/s) is the solution inlet velocity.

183 2.1.2 Air-side heat and mass transfer coefficient

184 According to [49], when air flow crosses a bundle of tubes with $Re_{D,max}$ in the range of 2000
 185 to 40000 and Pr over than 0.7, the heat transfer coefficient at the air side is given by:

$$186 \quad Nu_{air} \\ 187 \quad = 1.13C_1 Re_{D,max}^m Pr^{\frac{1}{3}} \quad (5)$$

188 Where C_1 and m can be obtained from [49], and $Re_{D,max}$ can be calculated by:

$$189 \quad Re_{D,max} = \frac{d_{h,air} u_{max}}{\nu} \quad (6)$$

190 Where u_{max} (m/s) is the maximum air velocity passing through the air channel, which can be
 191 calculated by:

$$192 \quad u_{max} = \frac{u_{air,i} d_{h,air}}{d_{h,air} - d_o} \quad (7)$$

193 $d_{h,air}$ (m) is the equivalent hydraulic diameter of the air channel, which can be calculated as:

$$194 \quad d_{h,air} = \frac{(1 - \varphi) d_c^2}{n_f d_o + d_c} \quad (8)$$

195 Where d_o (m) is the fiber outside diameter, d_c (m) is the module cross section diameter. n_f is
 196 the number of fibers included in the module, and φ is the packing fraction of the module, i.e.
 197 the ratio of the total fiber surface area to the PHFD module surface are,

$$198 \quad \varphi \\ 199 \quad = \frac{n_f \pi d_o^2}{\pi d_c^2} \quad (9)$$

200 As indicated by Zhang et al. [47], for the proposed PHFD configuration, at lower inlet air
 201 velocity, the air flow could be considered as laminar flow with the air side mass transfer
 202 correlation shown in the following equation:

$$203 \quad Sh_{air} = (14.06\varphi^4 - 29.21\varphi^3 + 22.59\varphi^2 - 7.71\varphi \\ 204 \quad + 1.03) Re^{0.33} Sc^{0.33} \tau_k \quad (10)$$

205 Where air side Schmidt number can be calculated as:

$$206 \quad Sc_{air} \\ 207 \quad = \frac{\mu_{air}}{\rho_{air} \psi_{air}} \quad (11)$$

208 Where μ_{air} (Pa • s) is the air dynamic viscosity, ρ_{air} (kg/m³) is the air density, and ψ_{air} (m²/s)
 209 is the moisture diffusivity in air and

$$210 \quad \tau_k = 0.882\tau_f - 0.535 \quad (12)$$

211 where τ_f is the fractal dimension of the fiber packing. For the irregular and regular packing,
 212 the value of τ_f is 1 and 2, respectively, and the general value is 1.6 to 1.9[48].

213 2.1.3 Overall heat and mass transfer coefficients

214 The overall heat and mass transfer resistance should take into account the air-side resistance,
 215 solution-side resistance and hollow fiber resistance. The calculation equations were described
 216 in detail by Zhang et al.[48]. The overall heat transfer coefficient (h_{ov}) and the overall mass

217 transfer coefficient (k_{ov}) are estimated as the sums of the individual resistances, as shown in
 218 the following equations:

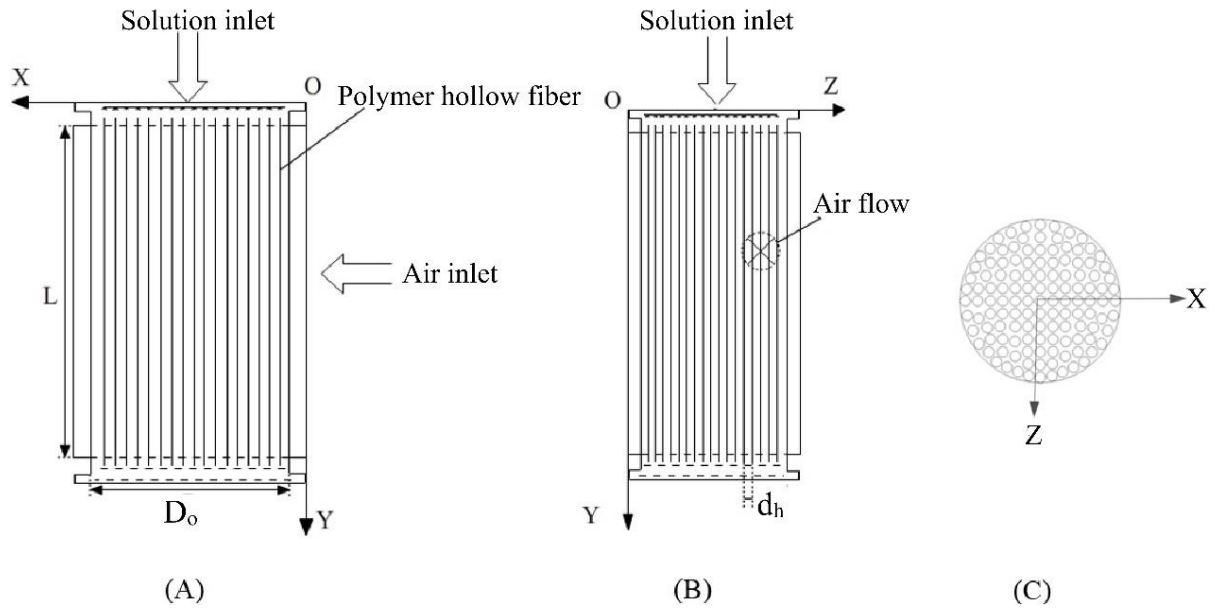
219

$$220 \quad h_{ov} = \left(\frac{1}{h_i} \left(\frac{d_o}{d_i} \right) + \frac{\delta}{\lambda_m} \left(\frac{d_o}{\bar{d}} \right) \right. \\ 221 \quad \quad \quad \left. + \frac{1}{h_o} \right)^{-1} \quad (13)$$

$$222 \quad k_{ov} = \left(\frac{1}{k_i} \left(\frac{d_o}{d_i} \right) + \frac{\delta}{\psi_m} \left(\frac{d_o}{\bar{d}} \right) \right. \\ 223 \quad \quad \quad \left. + \frac{1}{k_o} \right)^{-1} \quad (14)$$

224 where \bar{d} (m) is the average value of the fibers diameter, δ (m) is the thickness of the hollow
 225 fiber, d_o (m) and d_i (m) is the hollow fiber outside and inside diameter respectively. ψ_m (m²/s)
 226 is the effective mass diffusivity of the hollow fiber and λ_m (W/mK) is the effective thermal
 227 conductivity.

228 2.2 Heat and mass conservation equations



229

230 Fig. 2 The proposed polymer hollow fiber dehumidifier: (A) and (B) front view (C) section
 231 view

232 The proposed hollow fiber integrated crossflow desiccant dehumidifier is illustrated in Fig. 2.
 233 To simplify the numerical model, a series of basic assumptions were made:

- 234 (1) According to the numerical simulation presented by Ge et al.[28], when the fibers are
 235 arranged in staggered pattern with solution side Re number less than 2000, the solution side
 236 flow can be consider as fully developed and laminar.
- 237 (2) The physical properties of the air, solution, and the polymer hollow fiber, such as the
 238 specific heat, heat conductivity, etc. are constant.
- 239 (3) The model is based on a two-dimensional cross-flow, with each fluid flowing in a single
 240 direction.
- 241 (4) The axial water molecular diffusion, and the conduction of heat in the hollow fibers are

- 242 ignored, since the Peclet number in both channels is larger than 20 [50, 51].
 243 (5) Moisture condensates only in the liquid side, and the latent heat arising from phase changes
 244 is also released only in the liquid side.
 245 (6) All the fibers inside the PHFD module are assumed to be uniformly distributed, therefore,
 246 the solution will be distributed uniformly through each single fibers.

247 2.2.1 Air-side and solution-side governing equations

248 The solution-side heat and mass conservation equations are given as

$$249 \left(\frac{\dot{m}_{sol}}{n_{eq}d_i} \cdot \frac{\partial T_{sol}}{\partial y} \cdot C_{p,sol} \right) \\ 250 = h_{ov}(T_{air} - T_{sol}) + h_{fg} \cdot k_{ov} \cdot \rho_a (\omega_{air} - \omega_{sol}) \quad (15)$$

$$251 \frac{\dot{m}_{sol}}{n_{eq}d_i} \cdot \frac{\partial X_{sol}}{\partial y} = k_{ov} \cdot \rho_a \cdot (\omega_{air} - \omega_{sol}) \quad (16)$$

252 where $\dot{m}_{sol}(kg/s)$ is the solution mass flow rate, $T_{sol}(^{\circ}C)$ and $T_{air}(^{\circ}C)$ are the solution
 253 temperature and air inlet temperature respectively, ω_{air} (kg moisture/ kg air) and ω_{sol} (kg
 254 KCOOH/kg solution) are the air humidity ratio and desiccant solution mass fraction, and n_{eq}
 255 is the equivalent number of fibers, which can be calculated as:

$$256 n_{eq} = \frac{A_{tot}}{d_c L} \quad (17)$$

257 Where $d_c(m)$ is the dehumidifier module cross section diameter, $L(m)$ is the height of the
 258 hollow fiber model, $A_{tot}(m^2)$ is the total heat exchange area, which can be calculated as :

$$259 A_{tot} = n\pi d_o L \quad (18)$$

260
 261 The air-side governing equations are given as:

$$262 \frac{\dot{m}_{air}}{n_{eq}d_h} \cdot c_{p,air} \cdot \frac{\partial T_{air}}{\partial x} \\ 263 = h_{ov}(T_{sol} - T_{air}) \quad (19)$$

$$264 \frac{\dot{m}_{air}}{n_{eq}d_h} \cdot \frac{\partial \omega_{air}}{\partial x} + k_{ov}(\omega_{air} - \omega_{sol}) = 0 \quad (20)$$

265 where the $\dot{m}_{air}(kg/s)$ is the air flow rate, $c_{p,air}(J/kg K)$ is the air specific heat capacity.

266 2.2.2 Normalized equations

267 A range of dimensionless parameters can also be used:

268 The dimensionless temperature:

$$269 T^* = \frac{T - T_{air,i}}{T_{sol,i} - T_{air,i}} \quad (21)$$

270 The dimensionless humidity ratio:

$$271 \omega^* = \frac{\omega - \omega_{air,i}}{\omega_{sol,i} - \omega_{air,i}} \quad (22)$$

272 The dimensionless coordinates:

$$273 x^* = \frac{x}{d_c} \quad (23)$$

$$274 y^* = \frac{y}{L} \quad (24)$$

275 The dimensionless heat capacity ratios including sensible heat capacity ratio m_{sen} and latent
276 heat capacity ratio m_{lat} are defined below:

$$277 \quad m_{sen} = \frac{\dot{m}_{air} C_{p,air}}{\dot{m}_{sol} C_{p,sol}} \quad (25)$$

$$278 \quad m_{lat} = \frac{\dot{m}_{air} h_{fg} (\omega_{sol,i} - \omega_{air,i})}{\dot{m}_{sol} C_{p,sol} (T_{sol,i} - T_{air,i})} \quad (26)$$

279 The number of transfer unit is defined by:

$$280 \quad NTU = \frac{h_{ov} A_{tot}}{(\dot{m} c_p)_{air}} \quad (27)$$

281 And the number of mass transfer unit is defined by:

$$282 \quad NTU_m = \frac{\rho_{air} k_{ov} A_{tot}}{\dot{m}_{air}} \quad (28)$$

283 The normalized formulae for the heat and mass conservation on the air side are:

$$284 \quad \frac{\partial T_{air}^*}{\partial x^*} = NTU (T_{sol}^* - T_{air}^*) \quad (29)$$

$$285 \quad \frac{\partial \omega_{air}^*}{\partial x^*} = NTU_m (\omega_{sol}^* - \omega_{air}^*) \quad (30)$$

286 Similarly, the normalized formulae for the heat and mass conservation on the solution side are:

$$287 \quad \frac{\partial T_{sol}^*}{\partial y^*} = m_{sen} NTU (T_{air}^* - T_{sol}^*) + m_{lat} NTU_m (\omega_{air}^* - \omega_{sol}^*) \quad (31)$$

$$288 \quad \frac{\partial \omega_{sol}^*}{\partial y^*} = M \frac{\partial T_{sol}^*}{\partial y^*} \quad (32)$$

289 where M is related to the dimensionless solution humidity ratio and the dimensionless solution
290 temperature:

$$291 \quad M = E_T \frac{T_{sol,i} - T_{air,i}}{\omega_{sol,i} - \omega_{air,i}} \quad (33)$$

292 where E_T is related to the solution humidity ratio and the solution temperature, which is defined
293 as:

$$294 \quad E_T = \left. \frac{\partial \omega_{sol}}{\partial T_{sol}} \right|_{\bar{x}_{sol}} \quad (34)$$

295 with

$$296 \quad \omega_{sol} = 0.622 \frac{P_{sol}(X_{sol}, T_{sol})}{P_{atm} - P_{sol}(X_{sol}, T_{sol})} \quad (35)$$

297 where $P_{atm}(Pa)$ is the atmospheric pressure; $P_{sol}(Pa)$ is the solution's vapor pressure at a
298 particular concentration and temperature, which can be obtained by;

$$299 \quad P_{sol} = X_{sol} \cdot \exp^\gamma \cdot \exp^{P_{H_2O}} \quad (36)$$

300 where the parameters X_{sol} , γ , P_{H_2O} , are parameters related to desiccant solution and can be
301 found in[52]. The concentration of the desiccant solution can be calculated via the correlation
302 developed by Melinder [53], which relies on the temperature and density of the solution, as
303 shown below:

$$304 \quad X_{sol} = -253.148 + 0.04438563996 T_{sol} + 0.000162666247 T_{sol}^2 + 0.331709855 T_{sol} -
305 \quad 0.000079370267 \rho_{sol} \quad (37)$$

306 2.2.3 Boundary conditions

307 The solution side boundary conditions are:

$$308 T_{sol}^* = 1, \text{ at } y^*=0$$

$$309 \omega_{sol}^* = 1, \text{ at } y^*=0$$

310 The air side boundary conditions are:

$$311 T_{air}^* = 0, \text{ at } x^*=0$$

$$312 \omega_{air}^* = 0, \text{ at } x^*=0$$

313 2.4 Performance indices

314 Effectiveness is a key performance indicator of the dehumidifier. The sensible effectiveness
315 ε_{sen} , latent effectiveness ε_{lat} , and total effectiveness ε_{tot} were used to evaluate the proposed
316 model. The sensible effectiveness ε_{sen} is determined as the ratio of the air-temperature
317 difference between the area-averaged outlet and the inlet, to the difference between the inlet
318 solution temperature and the inlet air temperature (Eq. 38). The latent effectiveness ε_{lat} is the
319 ratio of the area-averaged inlet and outlet air humidity difference to the humidity difference
320 between the solution and the air at the inlet (Eq. 39);

$$321 \varepsilon_{sen} = \frac{T_{air,o} - T_{air,i}}{T_{sol,i} - T_{air,i}} \quad (38)$$

$$322 \varepsilon_{lat} = \frac{\omega_{air,o} - \omega_{air,i}}{\omega_{sol,i} - \omega_{air,i}} \quad (39)$$

323 The total effectiveness ε_{tot} is the ratio between the maximum and the actual energy transfer
324 rates, which could be expressed as in (Eq. 40);

325

$$326 \varepsilon_{tot} = \frac{\varepsilon_{sen} + h_{fg} \frac{(\omega_{air,i} - \omega_{sol,i})}{(T_{air,i} - T_{sol,i})} \varepsilon_{lat}}{1 + h_{fg} \frac{(\omega_{air,i} - \omega_{sol,i})}{(T_{air,i} - T_{sol,i})}} \quad (40)$$

327 The moisture removal rate M (kg/s) is also a very important performance indicator of the liquid
328 desiccant PHFD, and can be determined as:

$$329 M = \dot{m}_a (\omega_{air,i} - \omega_{air,o}) \quad (41)$$

330

331 2.5 Simulations

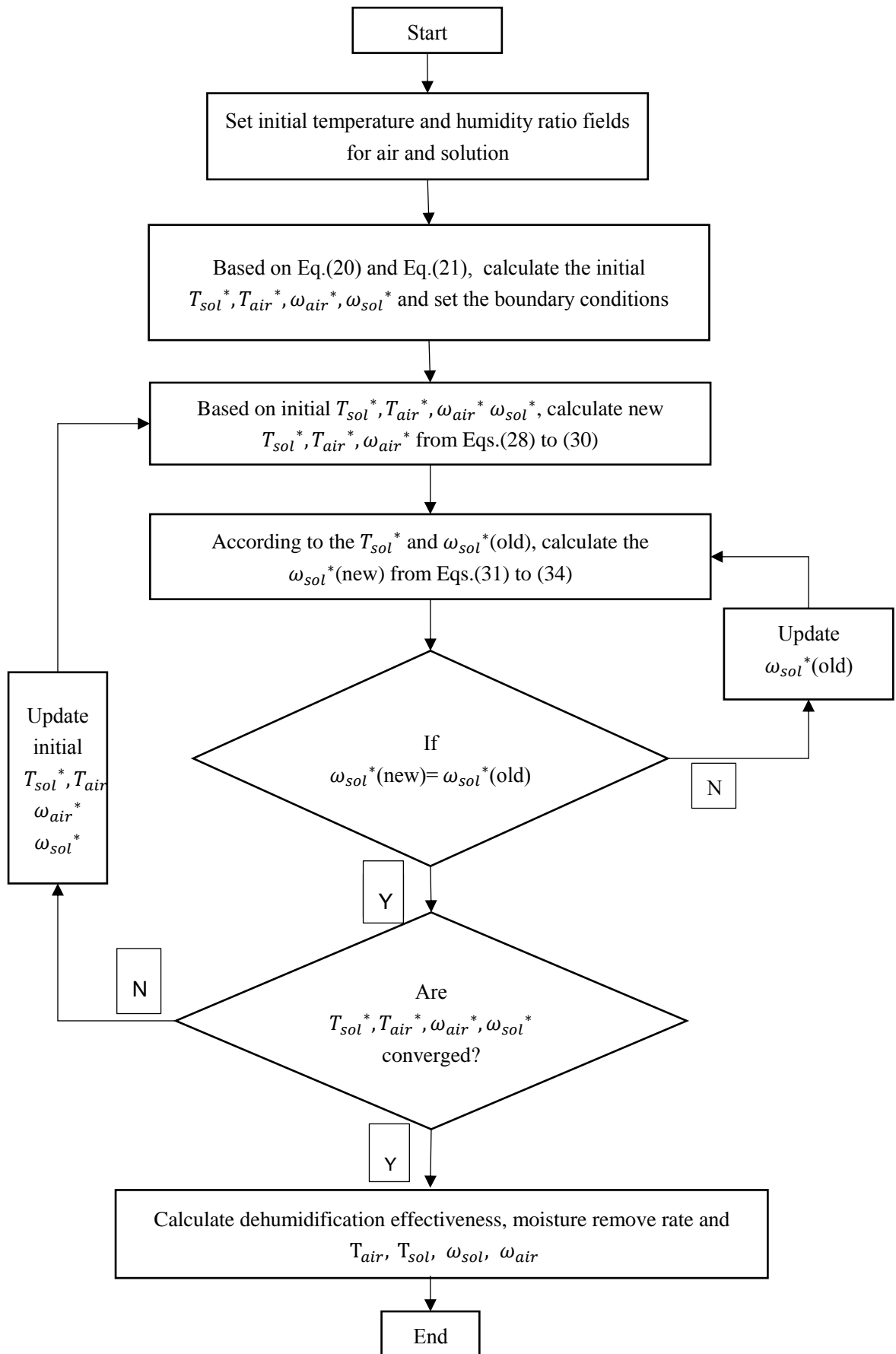
332 Eqs. (28) to (31) are the governing partial difference equations for the heat and mass transfer in
333 the proposed model. They are two-dimensional and two-variable partial differential equations.

334 A series of finite-differences iterations are performed in Matlab until the results converged. A

335 grid independence test was performed in order to optimize the grids. It was found that grids of

336 60×60 were sufficient for this study, as the difference of the results is less than 1% compared

337 to 60×120 grids. The process followed in this study is shown in the flowchart of Fig.3.



338

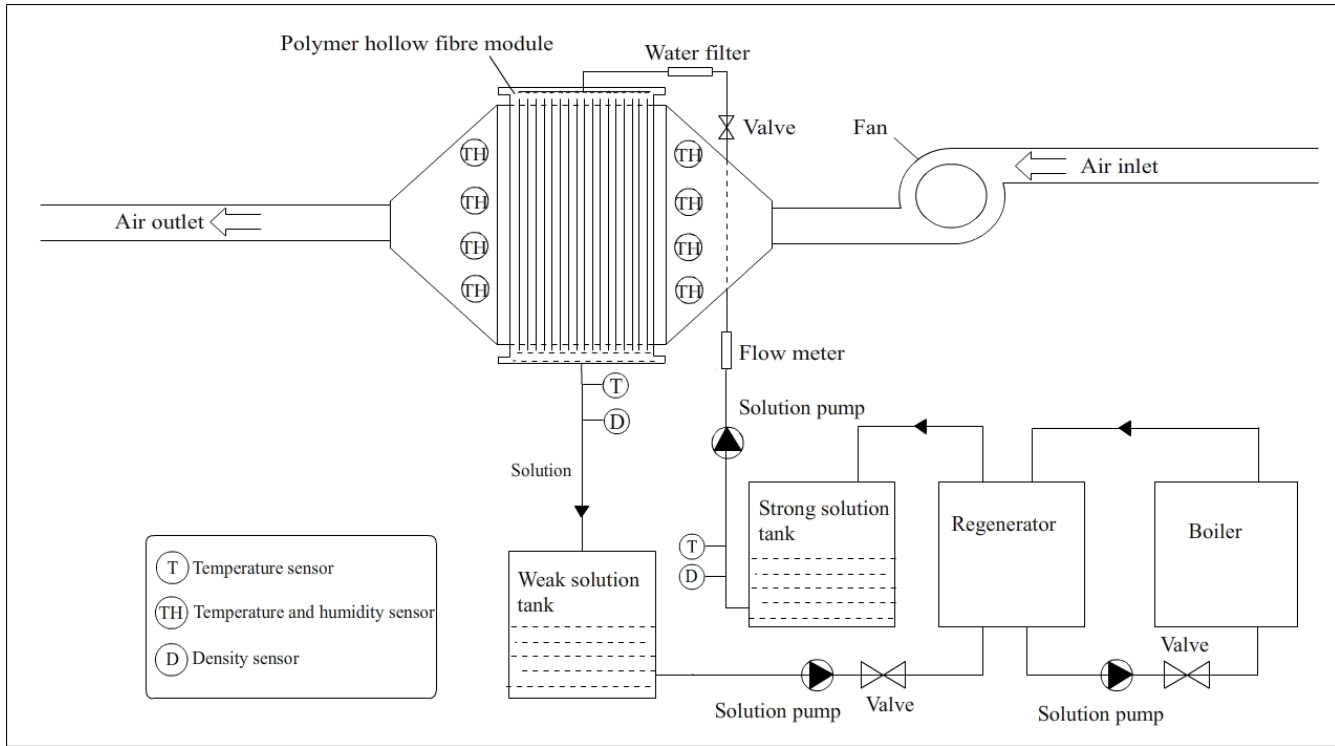
339

Fig.3. Flow chart for the simulation procedure

340 3. Experimental work

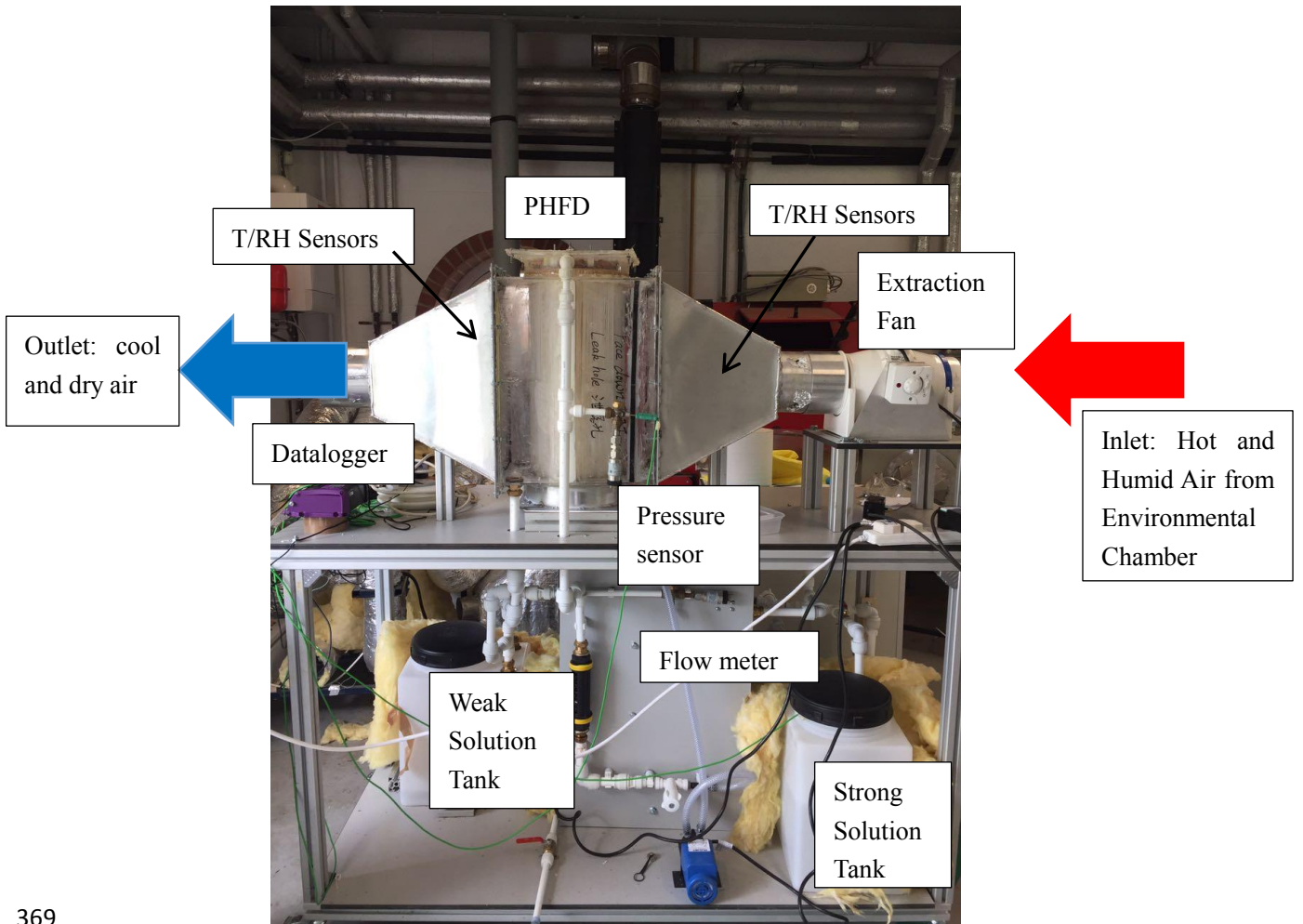
341 The experimental dehumidifier was assembled in the Marmot laboratory, University of
342 Nottingham, UK. The schematic diagram and the experimental set up can be found in Fig.4 (A)
343 and (B), respectively. The system includes the following major components: the polymer
344 hollow-fiber dehumidifier, the air channel, a fan, two circulation pumps, two solution tanks and
345 a water filter. The major component is the dehumidifier module with module cross section
346 diameter of 0.2m and length of 0.6m. 5500 porous hollow fibers were combined as a bundle
347 and attached on either end to a plastic disc by means of adhesive sealant. The polymer hollow-
348 fiber dehumidifier was further integrated in a transparent plastic box to allow interactions with
349 the incoming air. The aluminum air channel was attached to a centrifugal air fan with variable
350 frequency, connected in turn to the environmental chamber with supply of humid and hot air of
351 temperatures between 25°C and 40°C, and relative humidity of 0-75%. Two plastic tanks of an
352 eight-liter capacity carried the strong and weak solutions of the liquid potassium. Located at
353 the entrance of the PHFD, the water filter would help to eliminate any small particles entering
354 into the liquid desiccant solution. A ball valve and a flow-meter were fixed at the entrance to
355 the polymer hollow fiber module to control the solution flow rate inside the fibers. The physical
356 and geometrical properties of the PHFD are listed in Table 2.

357 The experiments were conducted as follows. The intake air from the environmental chamber
358 was directed inside the dehumidifier, once the environmental chamber had reached the required
359 temperature and relative humidity. The strong KCOOH solution was pumped from the strong
360 solution tank by a centrifugal pump (25W), to the desiccant solution inlet of the hollow fiber
361 module, where it was sprayed from the top of the PHFD and was left to trickle down into the
362 module. After being exposed to the inlet air, the dilute solution was collected into the relevant
363 weak solution tank. It was then pumped into the regenerator, constructed as an aluminum-plate
364 heat exchanger. Hot water (~80°C) was fed to the regenerator by a 3kW electrical boiler for the
365 purpose of desiccant regeneration. Once the solution concentration achieved its desired ratio, it
366 was returned to the strong-solution reservoir by a 25W single-phase centrifugal pump.



(A)

367
368



(B)

369
370

371 Fig. 4 Schematic diagram (A) and experimental set up (B) of the hollow fiber integrated
 372 liquid desiccant dehumidifier

373 Air temperature and humidity were measured by four dedicated monitoring devices (EK-H4,
 374 Sensirion, UK), which were placed by the inlet and the outlet of the air channel. The solution
 375 temperature was measured using K-type thermocouples. The air velocities in the air channel of
 376 the hollow fibre module were measured by a Testo anemometer. Its probe was distributed over
 377 several points around the outlet and inlet of the air tunnel. The dynamic pressure of the desiccant
 378 solution was measured by the Pressure transducers (Ge UNIK 5000). Finally, a DT500 data
 379 logger collected all the data from the above sensors. Detailed information about the measure
 380 sensors, for example, the measurement accuracy and measurement range are shown in Table 3.
 381 Uncertainty analysis of the experimental results was conducted following Moffat's method[54],
 382 and is shown in Fig. 5-12.

383 Table 2. Physical and transport properties of the polymer hollow-fiber dehumidifier

Property	Parameter	Values	Unit
Dehumidifier cross section diameter	d_c	0.20	m
Dehumidifier height	L	0.6	m
Number of fibers inserted	n_f	5500	
Fiber outside diameter	d_o	1.6	mm
Fiber inside diameter	d_i	1.4	mm
Pore size (nominal)		0.2	μm
Fibre porosity		0.6	
Packing density		832	m^2/m^3
Packing fraction	ϕ	0.32	
Fibre thermal conductivity	λ	0.17	W/mK
Solution concentration	X	57-67	%
Inlet air velocity	u_{air}	0.65-4.5	m/s
Solution mass flow rate	\dot{m}_{sol}	0.028-0.125	kg/s
Inlet air temperature	T_{air}	35-40	$^{\circ}\text{C}$
Inlet air relative humidity	ω_{air}	55-80	%
Specific heat of solution	C_{sol}	3.1	kJ/kg K
Dynamic viscosity of solution	μ_{sol}	5.1×10^{-3}	$\text{Pa} \cdot \text{s}$
Heat of evaporation	h_{fg}	2501	kJ/kg
Moisture diffusivity in air	ψ_{air}	2.82×10^{-5}	m^2/s
Effective mass diffusivity of the hollow fiber	ψ_m	1.2×10^{-5}	m^2/s
Water diffusivity in solution	ψ_w	0.3×10^{-2}	m^2/s
Number of heat transfer unit	NTU	0.46-4.4	
Number of mass transfer unit	NTU_m	0.28-2.8	

384

385

Table 3 Measurement devices and their accuracy

Instrumentation	Measured parameter	Measurement range	accuracy
Humidity and temperature sensors	Air (relative) humidity	0-90% RH	±2%
Humidity and temperature sensors	Air temperature	-40-125 °C	±0.3%
Testo thermo-anemometer	Air velocity	0–10 m/s	±5%
K-type thermocouple	Desiccant solution temperature	0-1100 °C	±0.75%
Datalogger DT500	Data Acquisition		±0.15%
Branna hydrometer 200 series	Solution density	1.0-1.6 g/m ³	±2%
Parker liquid flow indicator	Desiccant solution flow rate	0-5 litre/min	±5%

386

4. Results and discussion

387

4.1 Model validation

388

4.4.1 Experimental validation

389

390

391

392

393

394

395

396

397

398

The simulation results were validated against experimental results using 5 groups of experimentally obtained data. According to [49], since the ratio of hydraulic diameter of the air channel to the fiber outside diameter is equal to 2, the two parameters C_1 and m in Eq. (5) is chosen as 0.229 and 0.632, respectively. Under the various operating NTU and Cr^* conditions, the calculated and experimentally obtained outlet air temperature, specific humidity, outlet solution temperature, sensible effectiveness and latent effectiveness have been listed in Table 4 and Table 6. It is obvious that the proposed model matches well with the experimental results for both sensible effectiveness and latent effectiveness, with discrepancy in the range of 3.1-9.3% for sensible effectiveness and 2.5-8.9% for latent effectiveness. Therefore, this model in general can successfully predict the heat and mass transfer process in the PHFD.

399

400

401

402

403

404

405

406 Table 4 Comparisons between numerically obtained and experimentally obtained sensible
 407 effectiveness under various NTU ($Cr^*=0.13$)

Operating conditions		Parameters							
NTU	$T_{air,o}(exp)$	$T_{air,o}(num)$	Error(%)	$T_{sol,o}(exp)$	$T_{sol,o}(num)$	Error(%)	$\epsilon_{sen}(exp)$	$\epsilon_{sen}(num)$	Error(%)
0.4684	33.07	33.00	0.2	29.75	29.85	0.3	0.351	0.363	3.3
0.6012	32.74	32.59	0.5	29.86	29.93	0.2	0.4113	0.437	4.6
1.2764	31.19	31.32	0.4	30.27	30.21	0.2	0.693	0.668	3.1
3.045	30.29	30.21	0.3	30.59	30.67	0.3	0.856	0.927	7.6
4.4126	30.15	30.07	0.3	30.89	30.97	0.2	0.882	0.973	9.3

408 Table 5 Comparisons between numerically obtained and experimentally obtained latent
 409 effectiveness under various NTU_m ($m^*=0.75$)

Operating conditions		Parameters							
NTU_m	$\omega_{sol,o}(exp)$	$\omega_{sol,o}(num)$	Error(%)	$\omega_{air,o}(exp)$	$\omega_{air,o}(num)$	Error(%)	$\epsilon_{lat}(exp)$	$\epsilon_{lat}(num)$	Error(%)
0.2803	0.0117	0.0118	0.3	0.0192	0.0190	1.0	0.191	0.196	2.5
0.8318	0.0122	0.0125	2.4	0.0164	0.0160	2.4	0.478	0.514	7.0
1.3232	0.0124	0.0129	4.0	0.0149	0.0144	4.0	0.613	0.664	7.6
1.8631	0.0126	0.0132	4.8	0.0140	0.0135	3.5	0.702	0.748	6.5
2.8631	0.0127	0.0134	5.5	0.0135	0.0127	5.9	0.749	0.822	8.9

410

411 4.1.2 Analytical Validation

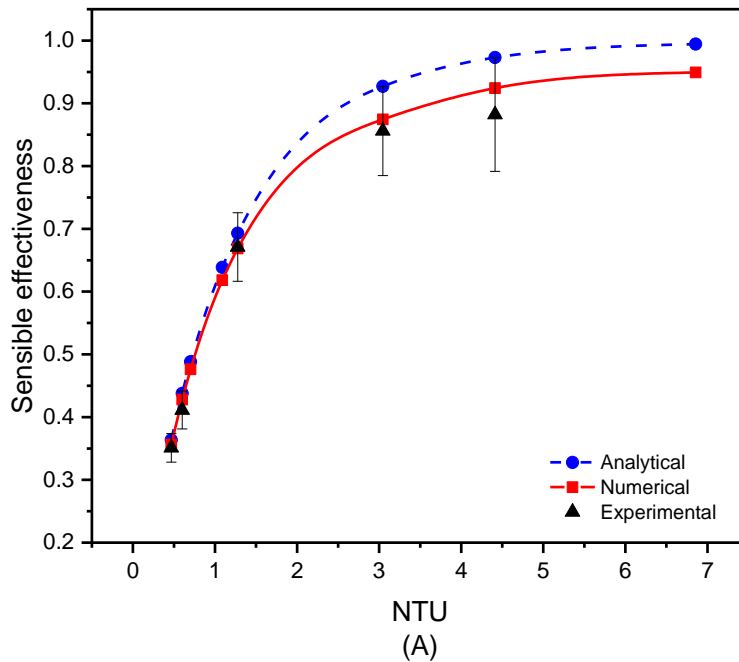
412 Analytical solutions for an enthalpy exchanger considering a membrane core have been
 413 reported in various works [55, 56]. According to these, the sensible effectiveness and latent

414 effectiveness of cross flow is given by the NTU- ϵ method. Those parameters are functions of
 415 four dimensionless parameters; the former are NTU and Cr^* and the latter are NTU_m and
 416 m^* [36]:

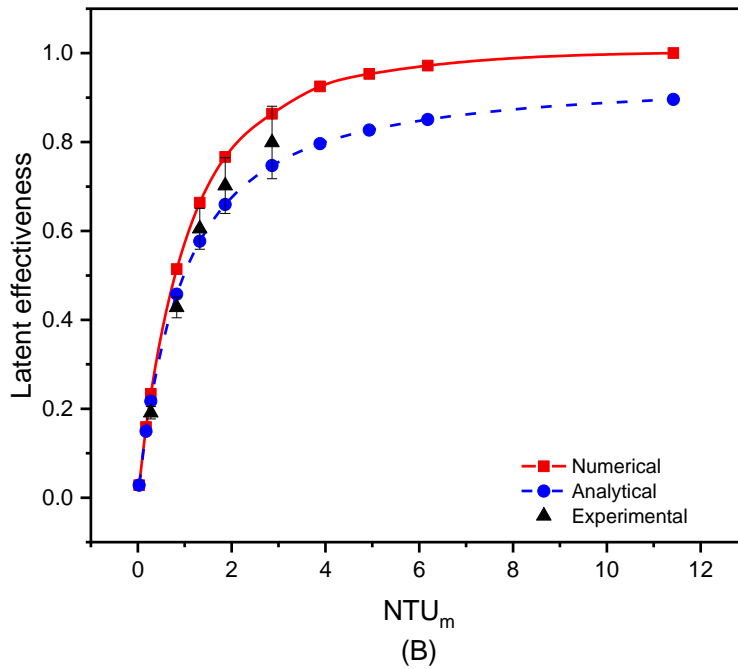
417 ϵ_{sen}
 418 $= 1 - \exp \left[\frac{\exp(-NTU^{0.78} Cr^*) - 1}{NTU^{-0.22} Cr^{*-1}} \right]$ (42)

419 $\epsilon_{lat} = 1 - \exp \left\{ \frac{NTU_m^{0.22}}{m^{*-1}} \left[\exp(-m^* NTU_m^{0.78}) \right. \right.$
 420 $\left. \left. - 1 \right] \right\}$ (43)

421 The results of the analytical solutions in Fig. 5 show a trend consistent with the numerical
 422 modelling results. As it can be seen in Fig. 5, a good agreement between numerical and
 423 experimental results occurs when the inlet air flow rate is less than 0.02kg/s. As the value of
 424 NTU and NTU_m increases, the two curves start to deviate. This is because the higher the NTU
 425 and NTU_m , the lower the air velocity and solution mass flow rate. With the 5500 hollow fibers
 426 imbedded in one module, the inner parts of the hollow fibers will have less opportunity to be
 427 exposed to the incoming air, leading to a decrease in heat transfer performance.



428



429
 430 Fig. 5 Variations of sensible effectiveness (A) and latent effectiveness (B) under various
 431 NTU_m based on experimental data, numerical results and analytical solutions.

432 4.1.3 Comparison with previous studies

433

434 This model is further compared with numerical results reported in the literature[57]. The
 435 validation considers a crossflow membrane dehumidifier operating under the inlet air
 436 temperature from 25.7 °C to 35.2 °C, specific humidity of 0.015kg/kg to 0.022kg/kg and inlet
 437 air mass flow rate of 7.55 to 15.65kg/h using LiCl as the desiccant solution. Table 6 shows the
 438 comparisons between Zhang’s model[57] and the model proposed in this paper under the above
 439 conditions. It can be found that the results of the outlet air temperature and the outlet solution
 440 temperature obtained from the model presented in this paper, are highly consistent with the
 441 results of Zhang’s model[57], with maximum discrepancy of 2.9% for the outlet solution
 442 temperature, and 1.6% for the outlet air temperature.

443

444 To summarize, the proposed numerical model was shown to be consistent with experimental
 445 results, the analytical solution, and results from the literature. Hence, this model could be
 446 adopted to analyze the working performance of the PHFD studied in this research.

447

448 Table 6 Comparisons between Zhang’s model [57] and the model proposed in this paper under
 449 the same conditions

Operating conditions				Parameters					
\dot{m}_{sol}	\dot{m}_{air}	$T_{air,i}$	$T_{sol,i}$	$T_{air,o}$		Error(%)	$T_{sol,o}$		Error(%)
				Zhang’s model	This model		Zhang’s model	This model	
9.69	6.36	33.9	24.9	25.99	25.65	1.3	32.44	32.90	1.4
9.75	8.67	35.2	25.3	28.04	27.72	1.1	36.89	37.51	1.8
9.66	12.22	34.9	25.2	29.58	29.54	0.1	37.78	38.52	1.9

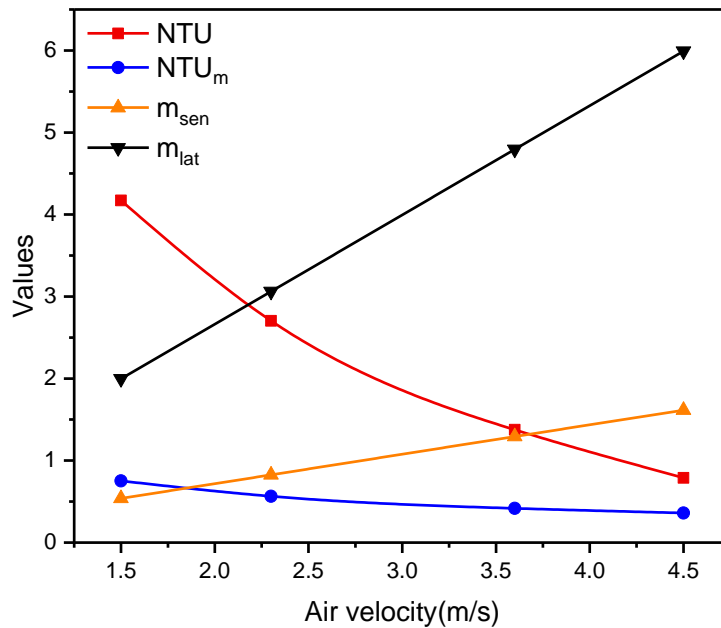
8.79	15.65	33.7	25.2	30.37	30.83	1.6	36.72	37.86	2.9
5.29	12.45	33.8	25.5	33.3	33.79	1.2	40.42	40.23	0.5
10.19	7.55	35.3	24.5	26.5	26.09	1.5	35.27	35.94	1.9
9.53	7.45	32.8	24.6	26.37	25.95	1.2	33.68	34.08	1.0
9.67	7.43	29.8	24.6	26.39	25.73	2.2	32.39	32.59	0.6
9.67	7.45	27.2	25.6	26.51	26.44	0.3	30	31.17	3.6
9.45	7.66	25.7	25.4	26.31	26.22	0.3	29.46	30.26	2.7

450

451 **4.2 Effect of the inlet air conditions**

452 According to the numerical analysis results, the inlet air conditions (i.e. inlet air velocity $V_{air,i}$,
453 and temperature $T_{air,i}$) are crucial parameters of the proposed PHFD. Fig 6-8 show the variations
454 of 4 parameters: sensible effectiveness, latent effectiveness, outlet air temperature and specific
455 humidity difference under various air velocities. As shown in Fig. 6, with increasing air velocity,
456 the latent heat capacity ratio (m_{lat}) and sensible heat capacity ratio (m_{sen}) will increase while the
457 NTU_m and NTU will decrease. As demonstrated in Fig. 7, a higher inlet air velocity will cause
458 a rise of the outlet air temperature and the specific humidity difference between the inlet and
459 the outlet air. This results in the increase of the sensible and latent effectiveness, as shown in
460 Fig.8. For example, at the inlet air relative humidity of 60% and dry bulb temperature of 35°C,
461 when the inlet air velocity increases from 1.5m/s to 4.5m/s, the specific humidity difference
462 between the inlet air and the outlet air are 0.0040kg/kg, 0.0030kg/kg, 0.0022kg/kg, 0.0018kg/kg
463 respectively. The sensible and latent effectiveness decreases from 0.381 to 0.03 and 0.383 to
464 0.178, respectively. This is because the higher air velocity leads to the reduction of the contact
465 duration between the incoming air and the desiccant solution inside the PHFD. This results in
466 less effective heat and mass transfer, which is reflected in the reduced sensible and latent
467 effectiveness, as shown in Fig.8.

468

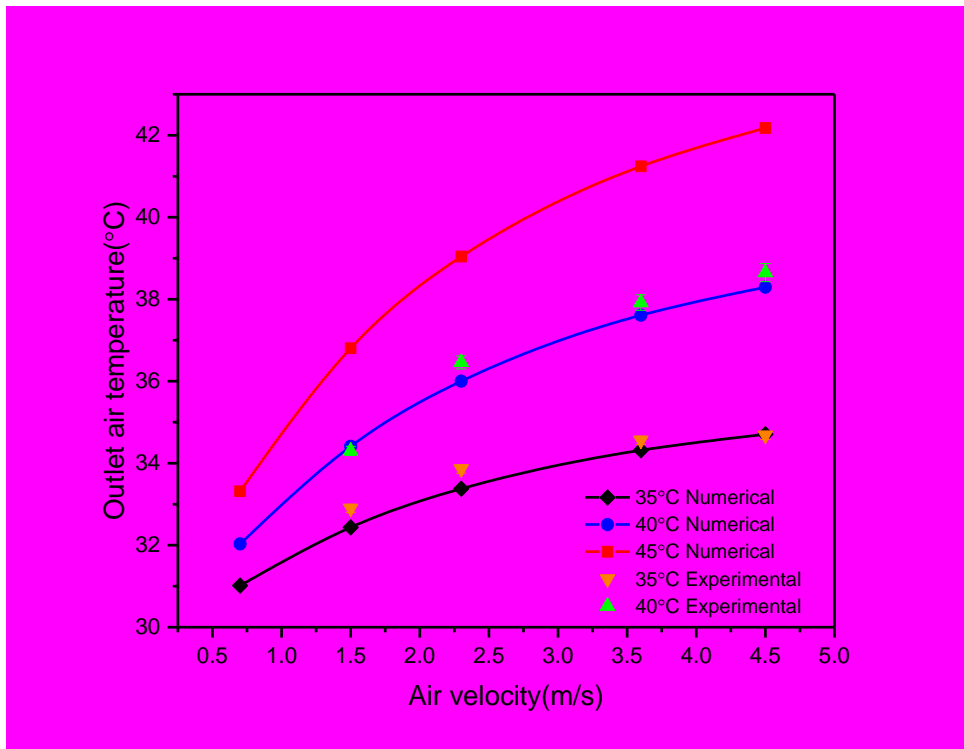


469

470 Fig. 6 The dimensionless parameters variations under different air velocities ($T_{air,i}= 35^{\circ}C$,

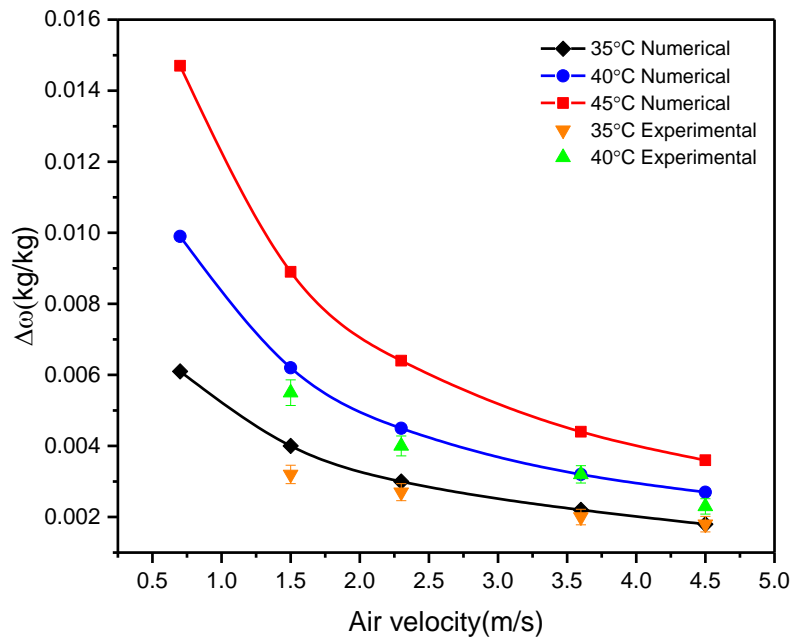
471
472

$T_{sol,i}=29.5^{\circ}\text{C}$, $\dot{m}_{sol,i}=0.028\text{kg/s}$, $\text{RH}_{air,i}=60\%$, $X_{sol}=62\%$



473
474
475

(A) (error bars in 35 degree C experimental results should be shown in this figure, the same as 40 degree C's error bar)

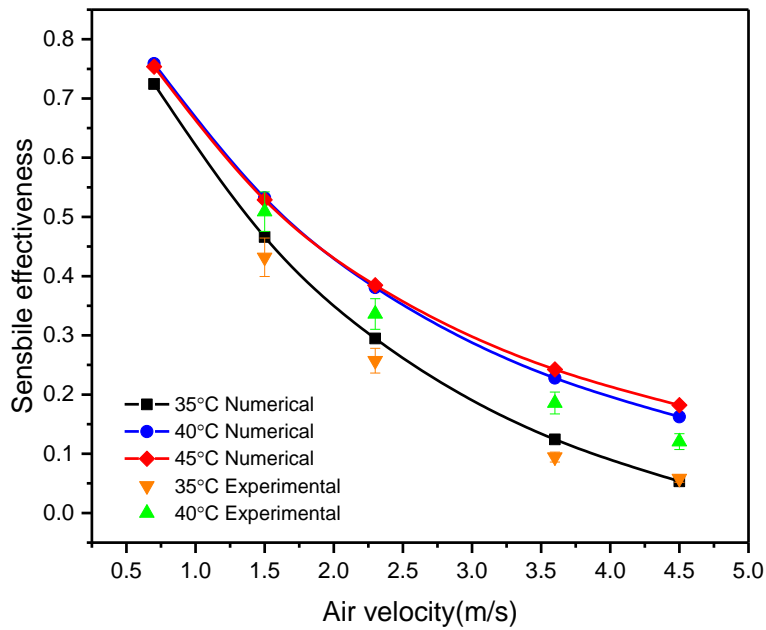


476
477

(B)

478 Fig. 7 The numerically obtained outlet air temperature (A), and specific humidity difference

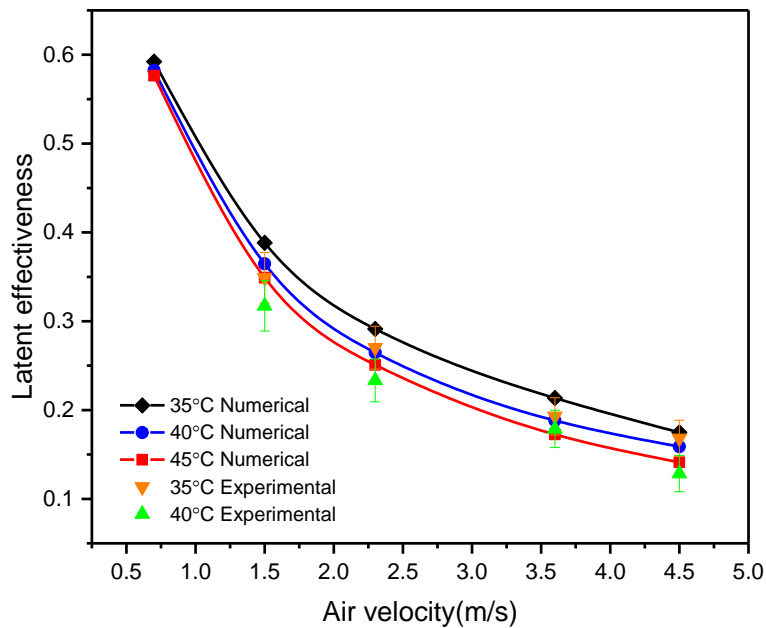
(B), under various air velocities ($T_{sol,i}=29.5^{\circ}\text{C}$, $\dot{m}_{sol,i}=0.028\text{kg/s}$, $\text{RH}_{air,i}=60\%$, $X_{sol}=62\%$)



480

481

(A)



482

483

(B)

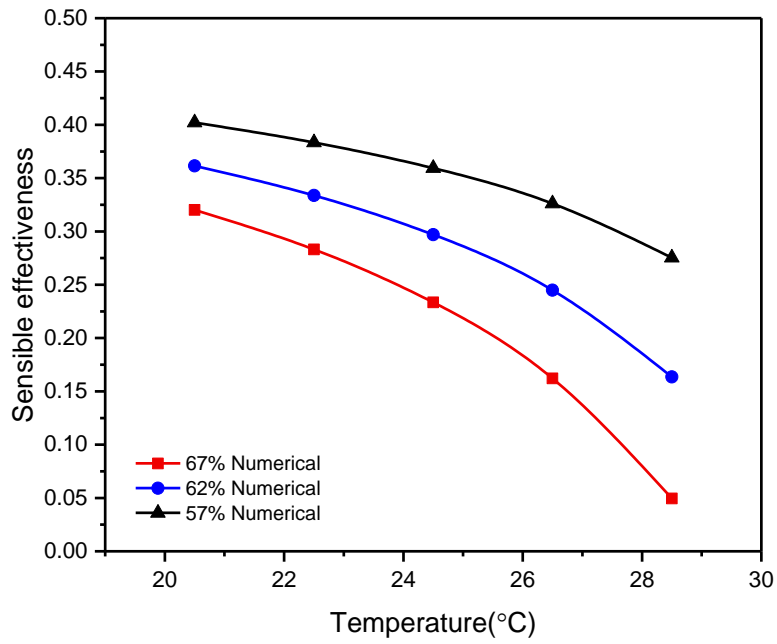
484 Fig. 8 The numerically obtained sensible effectiveness (A), and latent effectiveness (B), under
 485 different inlet air velocities ($T_{sol,i}=29.5^{\circ}\text{C}$, $\dot{m}_{sol,i}=0.028\text{kg/s}$, $\text{RH}_{air,i}=60\%$, $X_{sol}=62\%$)
 486

487 Further observation of the results shown in Fig. 8(A) reveals that at the fixed solution
 488 concentration and inlet air velocity, the sensible effectiveness will increase at a higher air

489 temperature. For instance, when the air velocity is fixed at 3.6m/s, for the inlet air temperature
490 of 35°C, 40°C and 45°C, the sensible effectiveness is 0.12, 0.23 and 0.24, respectively. In
491 contrast, as depicted in Fig. 8 (B), when the solution concentration and the inlet air velocity are
492 fixed, a higher inlet air temperature results in lower latent effectiveness. For instance, the latent
493 effectiveness only decreases by 1.6% and 1% respectively when the inlet air temperature
494 increases from 35°C to 40°C and 40 to 45°C at 0.7m/s air velocity, which is negligible. On the
495 contrary, $\Delta\omega$ increases with the improvement of inlet air temperature when the inlet air velocity
496 is fixed at 0.7m/s. The reason is that the increase of the inlet air temperature will lead to higher
497 specific humidity, while the inlet equilibrium humidity of the solution remains unchanged and
498 increases the vapor pressure difference indirectly.

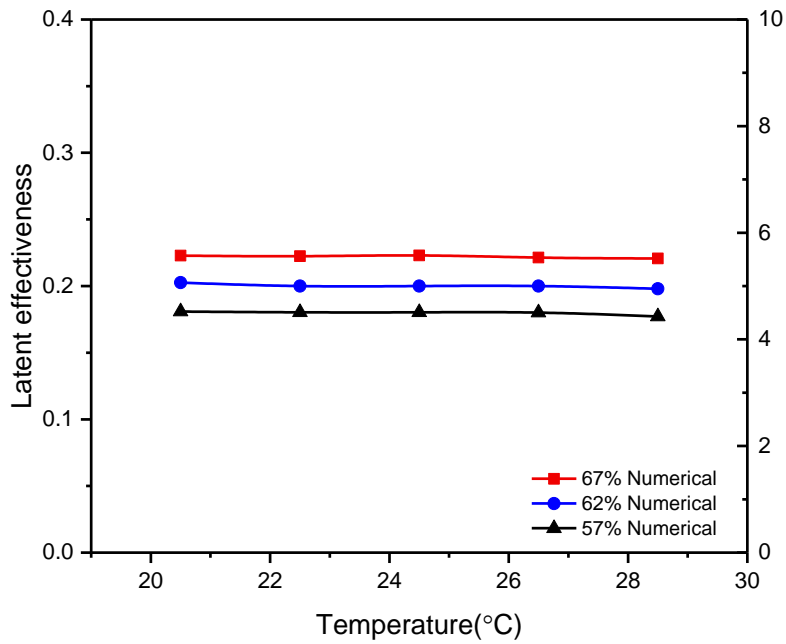
499 **4.3 Effect of the liquid desiccant solution inlet conditions**

500 The temperature of the solution and its concentration also play crucial roles in the
501 dehumidification performance. Fig.9 shows the variations of the sensible and latent
502 effectiveness under several inlet solution temperatures at various concentrations. As it can be
503 found from Fig.9 (A), the sensible effectiveness drops with the increase of the solution
504 temperature. For example, at a 57% concentration, the sensible effectiveness varies from 0.4 to
505 0.3 when the solution temperature changes from 20.5°C to 28.5°C. It should be noted that at
506 higher solution temperatures, high concentration solutions are more sensitive to temperature
507 changes. For instance, as the temperature of the solution rises from 26.5°C to 28.5 °C, the
508 sensible effectiveness at a 57% concentration drops by 15%. In contrast, when the concentration
509 is 62%, the corresponding decrease is 32%. In Fig.9(B), it can be seen that the latent
510 effectiveness almost remains constant as the solution temperature rises. For instance, at a 62%
511 concentration, the latent effectiveness is 0.203, 0.200, 0.200, 0.200, 0.198 at the solution
512 temperature of 20.5°C, 22.5°C, 24.5°C, 26.5°C, 28.5°C, respectively. This is because,
513 according to Eq. (35), the solution equilibrium humidity (K_{COOH}) is related to its temperature
514 and concentration. Although the vapor pressure will naturally increase with the solution
515 temperature, the solution equilibrium humidity will also increase, and will thus reduce both the
516 nominator and denominator of Eq. (35). In addition, lower solution concentration leads to lower
517 latent effectiveness, for example, at 26.5°C, the latent effectiveness is 0.22, 0.20, and 0.18 for
518 the concentration ratios of 67%, 62%, 57%, respectively.



519
520
521

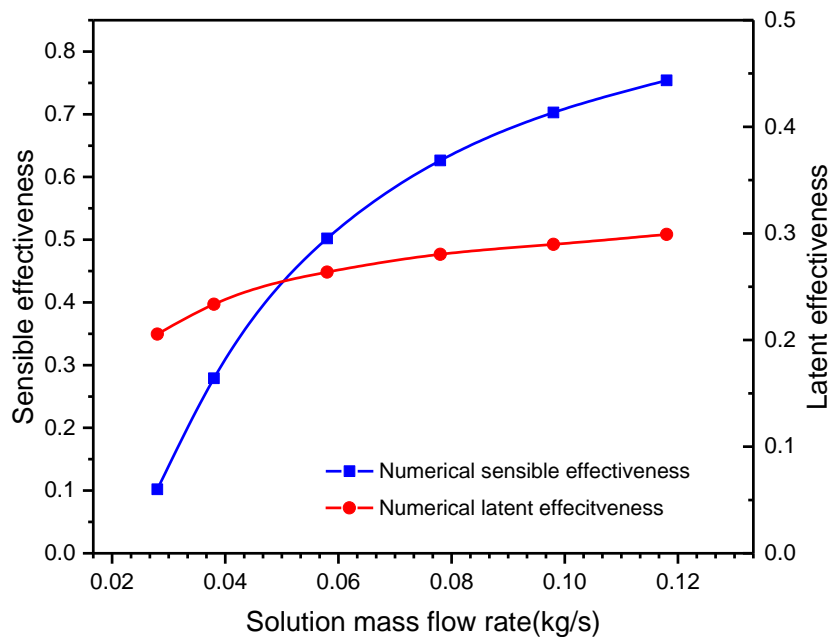
(A)



522
523
524
525
526

(B)

Fig. 9 Variations of sensible effectiveness (A), and latent effectiveness (B), for several inlet solution temperatures at various solution concentrations ($T_{air,i}=35^{\circ}C$, $RH_{air,i}=60\%$, $V_{air,i}=3.6m/s$, $\dot{m}_{sol,i}=0.028kg/s$)



527

528 Fig 10 Variations of latent and sensible effectiveness with the solution mass flow rate ($T_{air,i}=$
529 35°C , $T_{sol,i}= 29.5^{\circ}\text{C}$, $RH_{air,i}= 60\%$, $X_{sol}= 62\%$, $V_{air,i}= 3.6\text{m/s}$)

530 Fig.10 shows the relationship between solution mass flow rate and effectiveness, including
531 sensible effectiveness and latent effectiveness. With the increase of the solution mass flow rate,
532 the sensible effectiveness will increase dramatically. For instance, when the air mass flow rate
533 increases from 0.02kg/s to 0.012kg/s, the sensible effectiveness shows a 7.7 times increase.
534 This is because a higher solution flow leads to a lower average solution temperature, and the
535 outlet air temperature will decrease. As for the latent effectiveness, this will also increase with
536 the solution mass flow rate. For example, the sensible effectiveness only increases by 46%
537 when the solution flow rate rises from 0.02kg/s to 0.012kg/s. This is because the increase of the
538 solution mass flow will result in the lower average equilibrium vapour pressure of the desiccant
539 solution, and a higher mass transfer capacity will be obtained. It should be noted that when the
540 solution mass flow rate is over 0.08kg/s, the growth rate of both the sensible and latent effectiveness
541 will drop. As far as the sensible effectiveness is concerned, the reason for this is that the average
542 solution temperature has a limit value, which is infinitely close to the initial solution temperature
543 when the solution mass flow rate is much bigger than the air flow rate, hence the heat transfer driving
544 force becomes weaker. For the latent effectiveness, the larger the solution mass flow rate, the more
545 moisture will be absorbed by the desiccant, and the value of the air-specific humidity will be close
546 to the equilibrium specific humidity of the desiccant solution, hence the ability of absorbing the
547 moisture will become weaker.

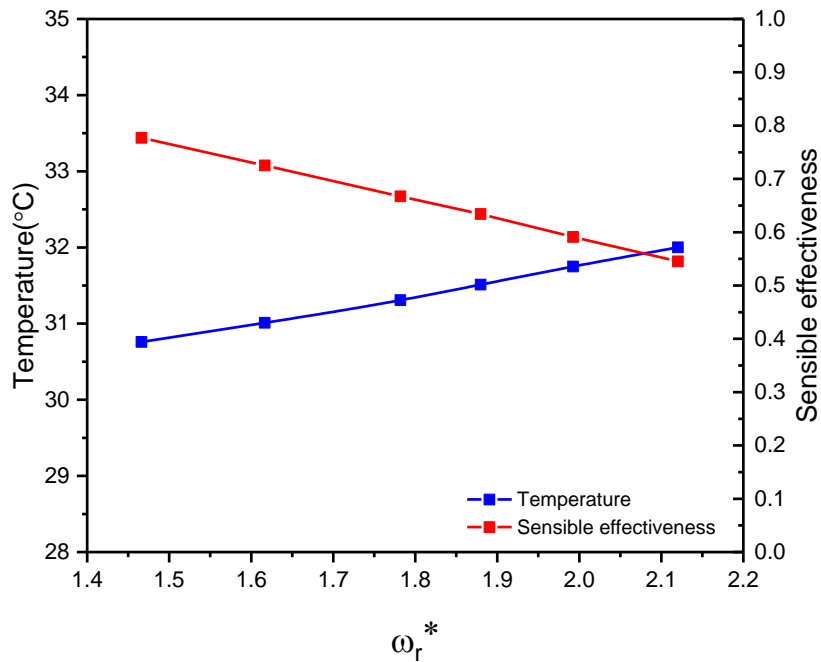
548 4.4 Effects of the dimensionless parameters

549 The influences of the air to solution specific humidity ratio ω_r^* on the outlet air temperature,
550 the sensible effectiveness, the specific humidity difference, the moisture removal rate, the latent
551 effectiveness, and the total effectiveness are demonstrated in Figs. 11-13. The other initial air
552 and solution conditions were invariable, the air velocity at the inlet was fixed at 0.7m/s, the

553 inlet air temperature was fixed at 35°C, and the inlet solution mass flow rate was 0.028 kg/s.
 554 As shown in Fig. 11, the air temperature at the outlet rises from 30.6°C to 31.8°C (an increase
 555 of 3.9%) and the sensible effectiveness drops from 0.79 to 0.57 (a fall of 22%) when the ω_r^*
 556 varies between 1.46 and 2.12. Inspection of Fig. 12 reveals that both the air specific humidity
 557 difference and the moisture removal rate both increase when the ω_r^* increases. For instance, the
 558 air specific humidity difference is 0.0053 kg/kg, 0.0065 kg/kg, 0.0079 kg/kg, 0.0089 kg/kg,
 559 0.0098 kg/kg and 0.0106 kg/kg at ω_r^* of 1.46, 1.62, 1.78, 1.88, 1.99 and 2.12, respectively, and
 560 the rate of moisture removal rised by 104% (from 0.21kg/s to 0.43kg/s) at each ω_r^* . The reason
 561 is that a higher ω_r^* reflects a higher water vapor pressure. No matter whether the inlet air
 562 specific humidity increases or the inlet solution concentration decreases, a greater vapor
 563 pressure difference between incoming air and desiccant solution is built. This leads to the
 564 solution attracting more moisture from the inlet air, which increases the specific humidity
 565 difference between the inlet air and the outlet air. When the desiccant solution absorbs more
 566 vapor, a higher amount of latent heat will be released. This results in a smaller temperature
 567 difference between the incoming air and the desiccant solution, which makes the temperature
 568 drop gradually.

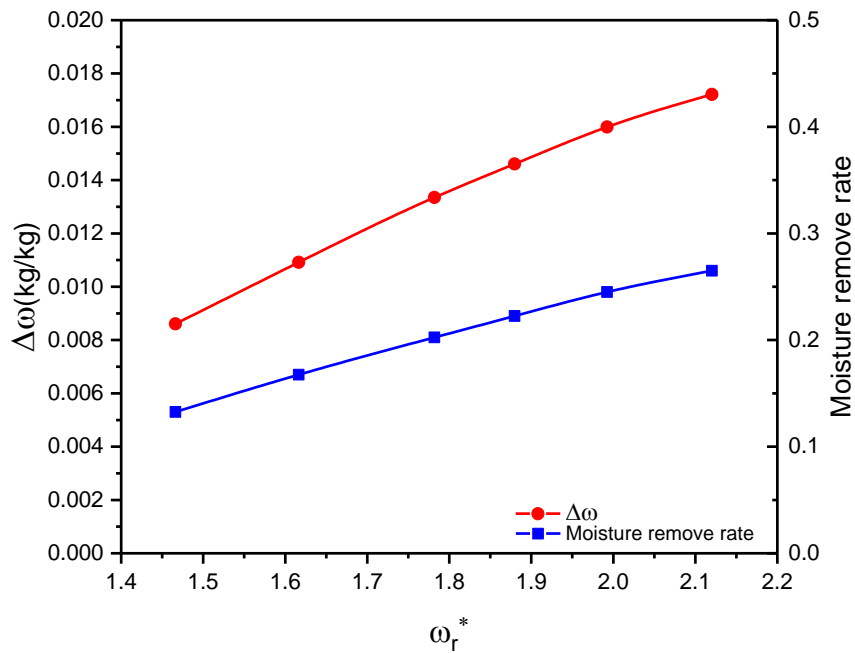
569

570 As shown in Fig. 13, the impact of the air to solution specific humidity ratio on the latent
 571 effectiveness is negligible. For example, the latent effectiveness remains around 0.61, when ω_r^*
 572 changes from 1.45 to 2.15. On the other hand, the total effectiveness decreases with the increase
 573 of ω_r^* . This is because although the air-specific humidity or solution equilibrium humidity
 574 increase dramatically with the rise of ω_r^* , the air specific humidity difference between the air
 575 and the solution at the inlet also grows. Thus, the latent and total effectiveness are not affected
 576 by ω_r^* .



577

578 Fig 11 Variation of the outlet air temperature and sensible effectiveness with the air to
 579 solution specific humidity ratio ($T_{air,i}= 35^\circ\text{C}$, $T_{sol,i}= 29.5^\circ\text{C}$, $\dot{m}_{sol,i}= 0.028\text{kg/s}$, $V_{air,i}= 3.6\text{m/s}$)

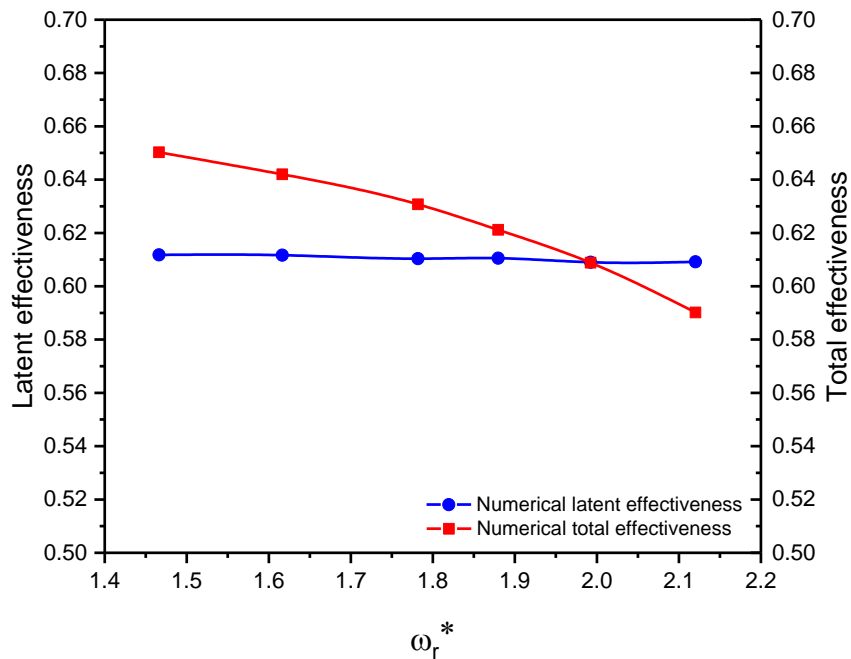


580

581

582

Fig 12 Variation of the specific humidity difference and moisture removal rate with the air to solution specific humidity ratio ($T_{air,i}=35^{\circ}C$, $T_{sol,i}=29.5^{\circ}C$, $\dot{m}_{sol,i}=0.028kg/s$, $V_{air,i}=3.6m/s$)



583

584

585

Fig 13 Variation of the latent effectiveness and total effectiveness with the air to solution specific humidity ratio ($T_{air,i}=35^{\circ}C$, $T_{sol,i}=29.5^{\circ}C$, $\dot{m}_{sol,i}=0.028 kg/s$, $V_{air,i}=3.6 m/s$)

586

587

588

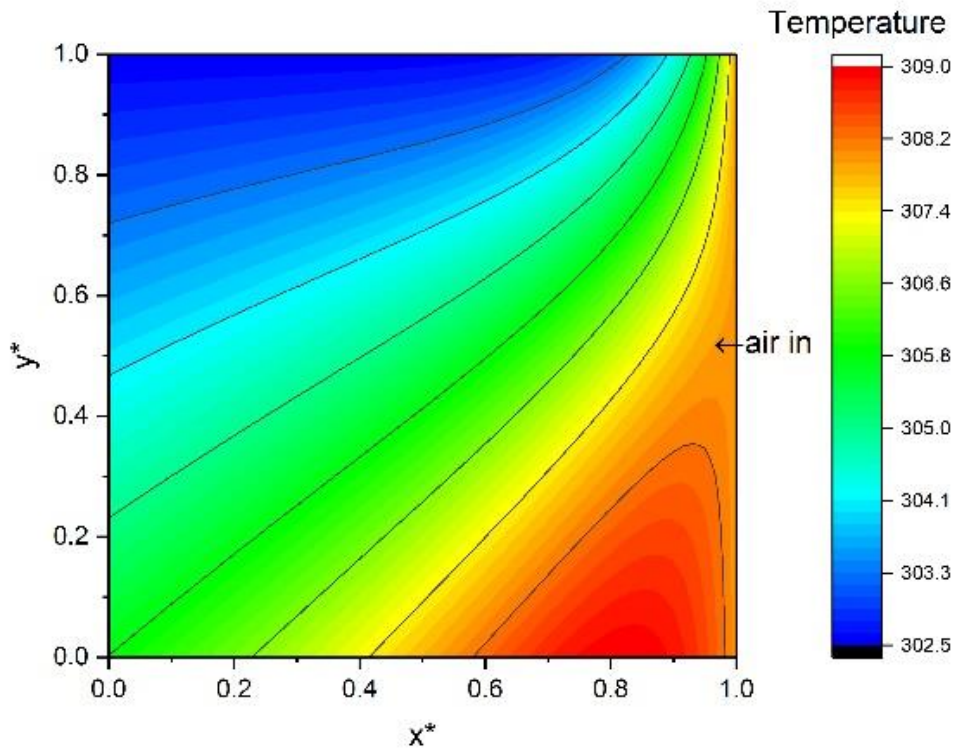
589

To summarize, the variation of air velocity has a strong impact on T_{ao} , ω_{ao} , NTU, NTU_m , m_{sen} , m_{lat} , and has a significant effect on the latent effectiveness and the sensible effectiveness. The sensible effectiveness and total effectiveness are less related to ω_r^* . The moisture removal rate and the sensible effectiveness also change significantly with the variations of ω_r^* . In addition,

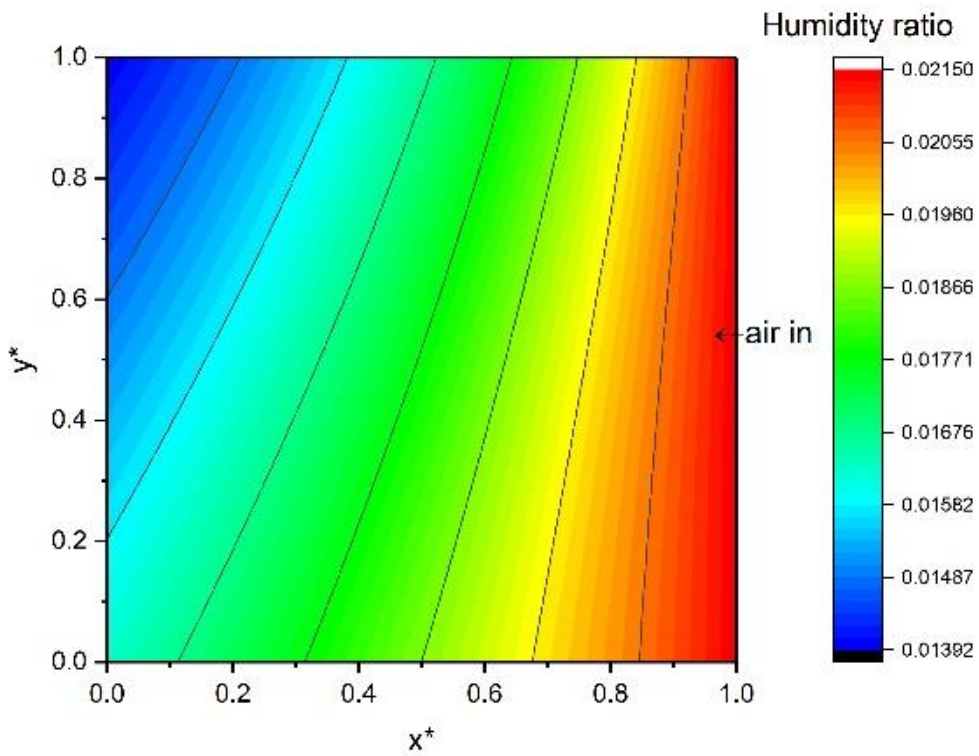
590 the change of air specific humidity difference and the inlet and outlet air temperature difference
591 are closely related to ω_r^* . This implies that changes of the ω_r^* within a certain range (i.e. 1.45
592 to 2.15) is preferable for increasing the dehumidification performance without reducing the
593 latent effectiveness.

594 **4.5 Temperature and humidity contour**

595 Temperature and humidity ratio contours of both the air and the solution are plotted in Figs.14-
596 15, based on the modeling results. The inlet air temperature, specific humidity ratio and mass
597 flow rate are 35°C, 0.0215kg/kg and 0.0407kg/s, respectively, and the inlet solution temperature
598 is 29.5°C , while the inlet equilibrium humidity ratio of the solution is 0.01076kg/kg, and the
599 solution mass flow rate is 0.028 kg/s. In Figs.14-15, the bottom boundary line indicates the
600 solution inlet and the right boundary line indicates the air inlet. Fig. 14 indicates that the air
601 specific humidity decreases from the inlet to the outlet. It is interesting to observe that the drop
602 rate of the air specific humidity slows down from the solution inlet to the solution outlet. This
603 is mainly because at the solution inlet, the solution has the lowest equilibrium humidity ratio,
604 which means that the solution can maximally absorb moisture from the incoming air. In contrast,
605 at the outlet, the desiccant solution has a much higher equilibrium humidity ratio. As for the air
606 flow, the temperature decreases along the x axis, and reaches the lowest temperature (top right
607 corner of the model) at nearly 29.5°C. It should also be noted that at the corner between solution
608 outlet and air inlet, the air temperature is slightly higher than the inlet temperature. This is due
609 to the accumulation of latent heat released by moisture, and sensible heat from the air, which
610 leads to the rise of the solution temperature as indicated in Fig. 14. As seen, the solution
611 temperature and equilibrium humidity ratio both increase from solution inlet to solution outlet
612 and reach the highest value (36.3°C and 0.01606kg/kg, respectively) at the corner between
613 solution outlet and air inlet of the model. The rate of change (from solution inlet to solution
614 outlet) slows down from the air inlet to the air outlet.



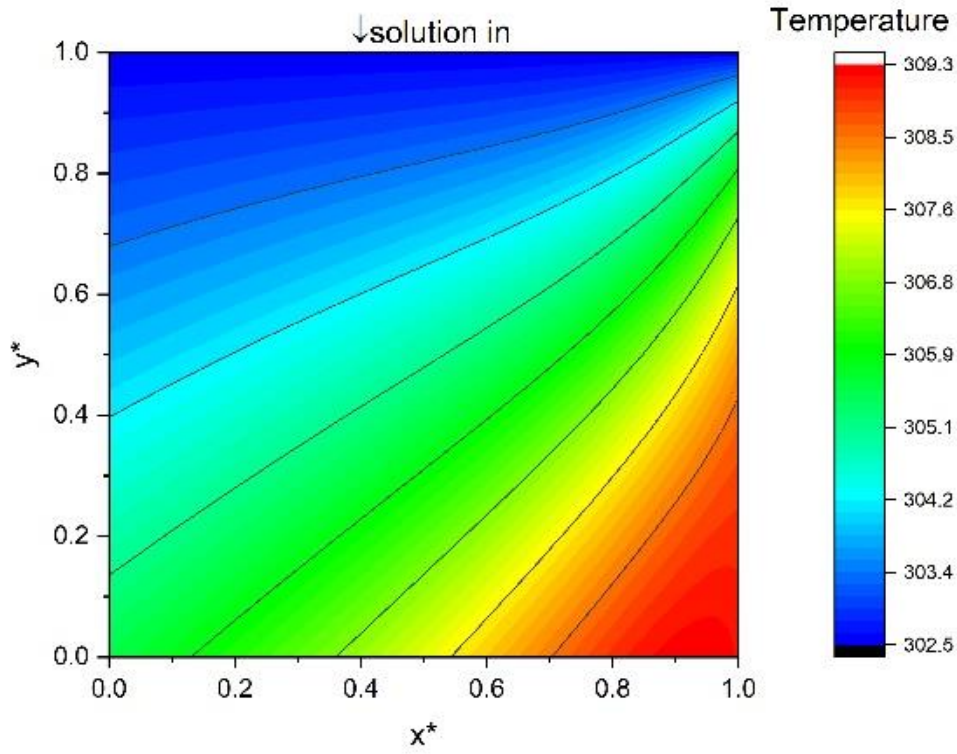
615



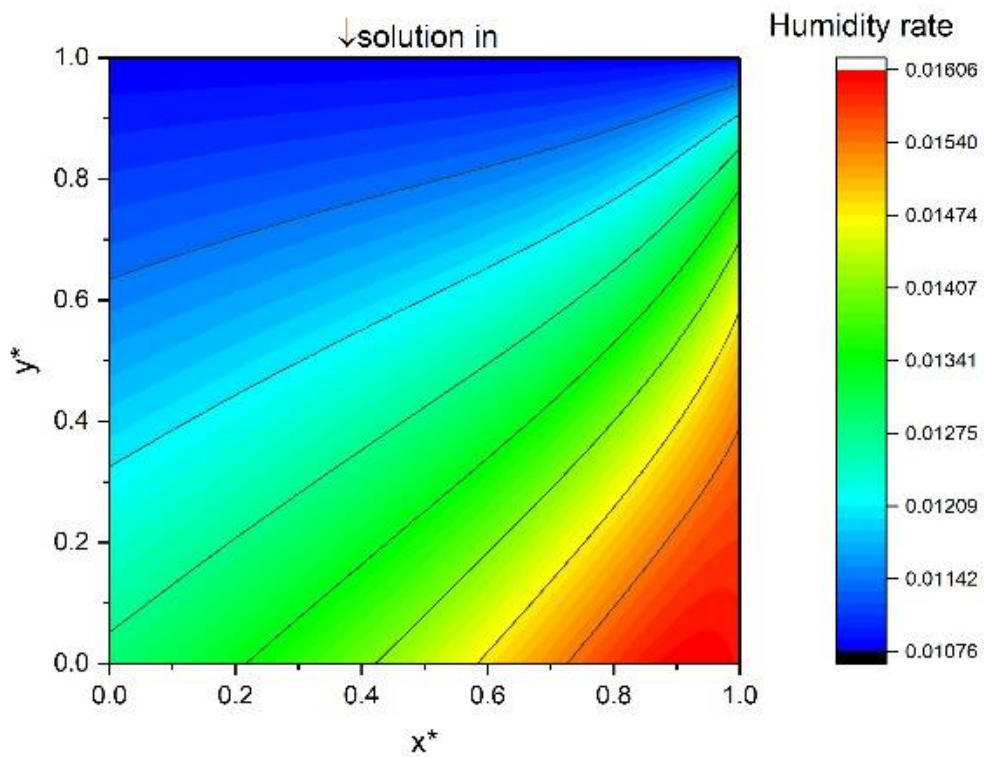
616

617

Fig. 14 Air temperature and humidity ratio contour



618



619

620

621

622 **5. Application**

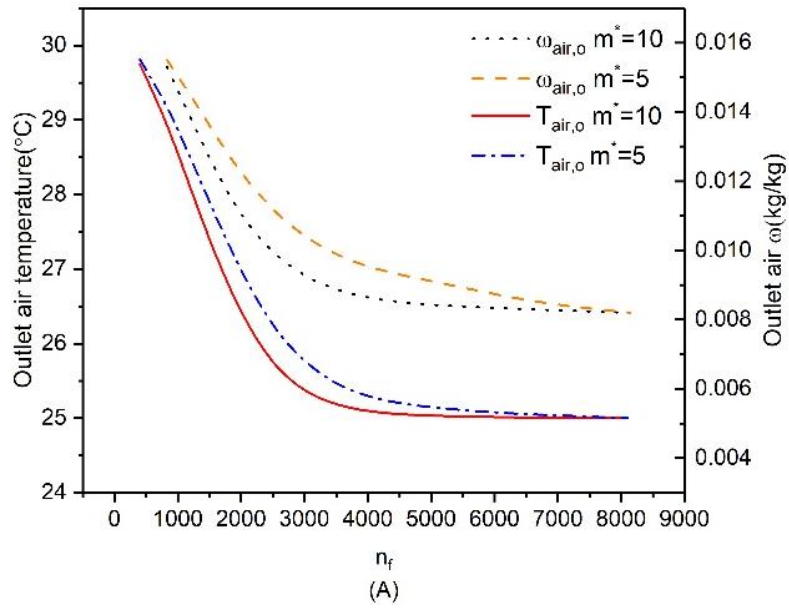
Fig. 15 Solution temperature and equilibrium humidity ratio contour

623

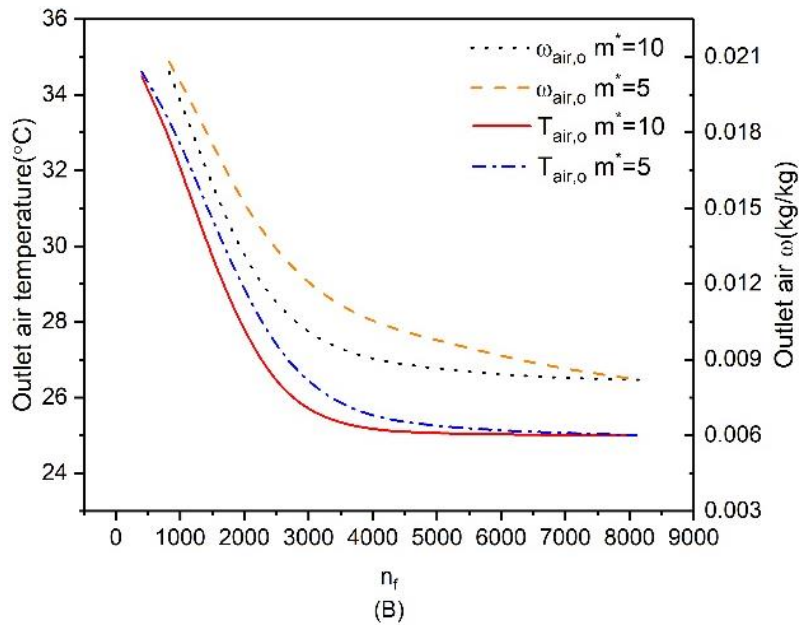
624 Fig. 16 depicts the simulated outlet air temperature and specific humidity as a function of the
625 number of fibers in the proposed liquid desiccant PHFD, with the inlet air RH=60% and inlet
626 air temperature fixed at 30°C, 35°C and 40°C, respectively. Calculations have been performed
627 based on the square cross section of the dehumidifier with fiber numbers increasing from 400
628 to 8100. Fig. 16 shows two different solutions to air mass flow ratios which represent the two
629 lowest air velocities ($\dot{m}_{sol}/\dot{m}_{air}=10$ and $\dot{m}_{sol}/\dot{m}_{air}=5$) applied in this research. Table 7
630 summarizes the outlet air conditions together with the sensible and latent effectiveness at the
631 inlet air temperature of 35°C, specific humidity of 0.0215kg/kg and solution inlet temperature
632 of 25°C. It can be seen that as the fiber number goes beyond 3000, the outlet air temperature,
633 as well as the sensible and latent effectiveness maintain roughly the same value. This indicates
634 that the optimum fiber number could be identified at around 3000 for lower air mass flow rate,
635 which is associated with more effective heat and mass transfer. As the inlet air mass flow rate
636 increases, the incoming air will have less time to be exposed to the desiccant solution, therefore
637 more fibers with larger surface areas are required to obtain higher sensible and latent
638 effectiveness.

639

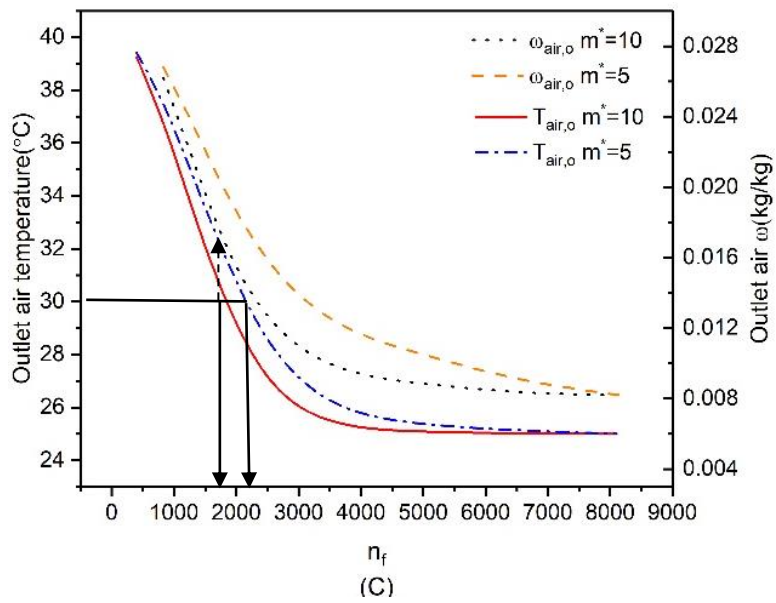
640 Fig. 16 and Table 7 can be useful in the practical design stage of polymer hollow fiber integrated
641 liquid desiccant dehumidification systems. It can help designers to obtain the desired number
642 of fibers by referring to the required outlet air temperature shown in Fig. 16 or based on the
643 required sensible and latent effectiveness indicated in Table 7, without having to repeat the
644 iterative simulations. For instance, as shown in Fig. 16 (C), with inlet air temperature at 40°C ,
645 approximately 1750 and 2380 fibers would be required to achieve the outlet air temperature of
646 30°C, respectively, for $\dot{m}_{sol}/\dot{m}_{air}=10$ and $\dot{m}_{sol}/\dot{m}_{air}=5$. At $\dot{m}_{sol}/\dot{m}_{air}=10$, the dehumidifier
647 with 1750 fibers will provide a total fiber surface area of 5.28m². This can be achieved by
648 inserting those fibers into a cylindrical module with the module cross section diameter equal to
649 0.28m. As the incoming air mass flow rate doubles ($\dot{m}_{sol}/\dot{m}_{air}=5$), in order to achieve the
650 same outlet temperature of 30°C, the required cylindrical module cross section diameter should
651 be increased to 0.36 m. This means that larger fiber surface area will be required at higher inlet
652 air mass flow rate. Similarly, by making use of Table 7, based on the required sensible and latent
653 effectiveness for different operational conditions, the designer could easily select the relevant
654 $\dot{m}_{sol}/\dot{m}_{air}$ and fibers number.



655



656



657

658 Fig. 16 The variations of outlet air temperature and specific humidity under various fiber
659 numbers with $\dot{m}_{sol}/\dot{m}_{air}=10$ and $\dot{m}_{sol}/\dot{m}_{air}=5$ and inlet air temperature of (A) $T_{air,i} =$
660 30°C (B) $T_{air,i} = 35^{\circ}\text{C}$ (C) $T_{air,i} = 40^{\circ}\text{C}$

661

662 Table 7 Variations of sensible effectiveness, latent effectiveness and outlet air conditions under
663 various fiber numbers and $\dot{m}_{sol}/\dot{m}_{air}$ ratio ($T_{air,i} = 35^{\circ}\text{C}$, $\omega_{air,i}=0.0215\text{kg/kg}$, $T_{sol,i}=25^{\circ}\text{C}$)

Number of fibers in the module	Inlet air mass flow rate	Mass flow rate ratio between inlet solution and inlet air	Outlet air conditions and associated effectiveness				
			$T_{air,o}(^{\circ}\text{C})$	$T_{sol,o}(^{\circ}\text{C})$	$\omega_{air,o}(\text{kg/kg})$	ϵ_{sen}	ϵ_{lat}
400	0.0087	10	34.49	25.30	0.0204	0.051	0.083
	0.0174	5	34.61	25.40	0.0208	0.039	0.053
	0.087	1	34.80	27.62	0.0213	0.020	0.015
	0.174	0.5	34.85	26.06	0.0214	0.015	0.008
900	0.0087	10	32.65	25.74	0.0172	0.235	0.323
	0.0174	5	33.19	26.09	0.0186	0.181	0.218
	0.087	1	34.10	30.07	0.0205	0.090	0.075
	0.174	0.5	34.36	28.10	0.0209	0.064	0.045
1600	0.0087	10	29.08	26.13	0.0129	0.592	0.647
	0.0174	5	30.24	26.81	0.0151	0.476	0.481
	0.087	1	32.60	31.32	0.019	0.240	0.188
	0.174	0.5	33.38	30.68	0.02	0.162	0.113
2500	0.0087	10	26.02	26.32	0.0101	0.898	0.857
	0.0174	5	27.03	27.26	0.0122	0.797	0.699
	0.087	1	30.41	31.83	0.0174	0.459	0.308
	0.174	0.5	31.90	32.73	0.0189	0.310	0.195
3600	0.0087	10	25.16	26.39	0.009	0.984	0.940
	0.0174	5	25.56	27.45	0.0122	0.944	0.827
	0.087	1	28.19	32.07	0.016	0.681	0.414
	0.174	0.5	30.05	33.86	0.018	0.495	0.263
4900	0.0087	10	25.05	26.42	0.0086	0.995	0.970
	0.0174	5	25.24	27.52	0.0097	0.976	0.887
	0.087	1	26.83	32.46	0.0149	0.817	0.496
	0.174	0.5	28.32	34.42	0.0172	0.668	0.323
6400	0.0087	10	25.01	26.49	0.0083	0.999	0.992
	0.0174	5	25.09	27.67	0.0088	0.991	0.955
	0.087	1	26.32	33.31	0.0132	0.868	0.624
	0.174	0.5	27.52	35.31	0.0157	0.748	0.436
8100	0.0087	10	25.00	26.56	0.0082	1.000	1.000
	0.0174	5	25.00	27.90	0.0082	1.000	1.000
	0.087	1	26.00	34.69	0.0103	0.900	0.842
	0.174	0.5	27.15	37.57	0.0121	0.785	0.707

664

665 6. Conclusions

666

667 This paper has reported a numerical model for a novel hollow fiber liquid desiccant
668 dehumidification system. A thorough validation demonstrated that the modelled outlet
669 parameters (temperature and specific humidity) for both the processed air and desiccant
670 solution, and the heat and mass transfers under various testing situations were consistent with
671 experimental results, analytical solutions, and results from the literature. Following its
672 successful validation, the model was then used to predict the working performance of the
673 dehumidifier. The effect of inlet parameters (inlet air velocity, inlet air specific humidity, inlet
674 solution temperature, inlet solution concentration, inlet solution mass flow rate) and the air to
675 solution specific humidity ratio on the sensible effectiveness, latent effectiveness and total
676 effectiveness were parametrically assessed. The relationship between NTU and the sensible
677 effectiveness, NTU_m and the latent effectiveness were also investigated. In addition, the
678 temperature and humidity ratio contour for the air and solution were studied. The main
679 conclusions of this paper can be summarized as follows:

680 (1) The effects of Cr^* and NTU, m^* and NTU_m on the sensible effectiveness and latent
681 effectiveness are obvious. The sensible effectiveness has changed remarkably (from 0.35 to 1)
682 with the increase of NTU in the range of 0.47 to 7 ($Cr^* = 0.13$). Meanwhile, the latent
683 effectiveness has also changed remarkably with the increase of NTU_m in the range of 0 to 12,
684 when m^* is 0.75.

685 (2) The increase in inlet air velocity will lead to the drop in sensible effectiveness, latent
686 effectiveness, the inlet and outlet air temperature difference, and the inlet and outlet air relative
687 humidity difference. As the incoming air velocity increases in the range of 1.5m/s to 4.5m/s,
688 the sensible effectiveness drops from 0.74 to 0.08, and latent effectiveness decreases from 0.58
689 to 0.14. The sensible effectiveness is more sensitive to the solution inlet temperature, solution
690 mass flow rate and solution concentration. The influences of the solution mass flow rate and
691 the solution concentration on the latent effectiveness are less important in comparison with the
692 sensible effectiveness.

693 (3) The moisture removal rate and air humidity ratio difference substantially grow with the
694 increase of the ω_r^* . As the ω_r^* increases from 1.45 to 2.15, the sensible effectiveness decreases
695 from 0.77 to 0.54, while the total effectiveness drops from 0.59 to 0.65. The changing ω_r^* has a
696 very limited effect on the latent effectiveness.

697 (4) The increase of solution inlet temperature leads to a drop of sensible effectiveness, while
698 the latent effectiveness remains more or less constant. For instance, as the solution inlet
699 temperature rises from 20.5°C to 28.5°C, the sensible effectiveness declines from 0.37 to 0.17.
700 Hence, a good way to achieve higher sensible effectiveness without affecting the latent
701 effectiveness could be by decreasing the solution concentration.

702 (5) At 62% solution concentration, the latent effectiveness is about 0.47 when the inlet air
703 velocity and solution mass flow rate is 0.087kg/s, which is comparable to the value obtained
704 from the literature when LiCl was the desiccant[57]. Therefore, in order to achieve a similar
705 dehumidification effect as in that case, a higher concentration of KCOOH desiccant solution
706 should be used.

707 (6) The influence of fiber numbers on the dehumidification effectiveness, outlet air temperature
708 and relative humidity have been analyzed and the results have been summarized in a user-

709 friendly table format. Without performing the iterative modelling, this Table can offer guidance
710 to the designer for selecting the relevant solution to air mass flow ratio and fibers number,
711 according to the required dehumidification effectiveness of the PHDF.

712

713

714 **Acknowledgement**

715 The authors greatly appreciate the financial contributions from the British funding body,
716 Innovate UK (project code: 131821).

717

718 **References**

719

720 1. Artola, I., *Boosting Building Renovation: What Potential and Value for Europe? : Study.*

721 2016: European Parliament.

722 2. Isaac, M. and D.P. van Vuuren, *Modeling global residential sector energy demand for*

723 *heating and air conditioning in the context of climate change.* Energy Policy, 2009.

724 **37(2):** p. 507-521.

725 3. Hitchin, R., C. Pout, and P. Riviere, *Assessing the market for air conditioning systems*

726 *in European buildings.* Energy and Buildings, 2013. **58:** p. 355-362.

727 4. Chua, K.J., et al., *Achieving better energy-efficient air conditioning – A review of*

728 *technologies and strategies.* Applied Energy, 2013. **104:** p. 87-104.

729 5. Chen, X., et al., *Experimental investigations of polymer hollow fibre integrated*

730 *evaporative cooling system with the fibre bundles in a spindle shape.* Energy and

731 Buildings, 2017. **154:** p. 166-174.

732 6. Chen, X., et al., *A novel evaporative cooling system with a polymer hollow fibre spindle.*

733 Applied Thermal Engineering, 2018. **132:** p. 665-675.

- 734 7. Peng, D. and X. Zhang, *An analytical model for coupled heat and mass transfer*
735 *processes in solar collector/regenerator using liquid desiccant*. Applied Energy, 2011.
736 **88**(7): p. 2436-2444.
- 737 8. Li, X., et al., *Dynamic modeling of a liquid desiccant dehumidifier*. Applied Energy, 2016.
738 **180**: p. 435-445.
- 739 9. Xiao, F., G. Ge, and X. Niu, *Control performance of a dedicated outdoor air system*
740 *adopting liquid desiccant dehumidification*. Applied Energy, 2011. **88**(1): p. 143-149.
- 741 10. Keniar, K., K. Ghali, and N. Ghaddar, *Study of solar regenerated membrane desiccant*
742 *system to control humidity and decrease energy consumption in office spaces*. Applied
743 Energy, 2015. **138**: p. 121-132.
- 744 11. Gao, W.Z., et al., *Experimental study on partially internally cooled dehumidification in*
745 *liquid desiccant air conditioning system*. Energy and Buildings, 2013. **61**: p. 202-209.
- 746 12. Yin, Y., et al., *Experimental study on a new internally cooled/heated*
747 *dehumidifier/regenerator of liquid desiccant systems*. International Journal of
748 Refrigeration, 2008. **31**(5): p. 857-866.
- 749 13. Luo, Y., et al., *Experimental study of internally cooled liquid desiccant dehumidification:*
750 *Application in Hong Kong and intensive analysis of influencing factors*. Building and
751 Environment, 2015. **93**: p. 210-220.
- 752 14. Bansal, P., S. Jain, and C. Moon, *Performance comparison of an adiabatic and an*
753 *internally cooled structured packed-bed dehumidifier*. Applied Thermal Engineering,
754 2011. **31**(1): p. 14-19.

- 755 15. Song, X., L. Zhang, and X. Zhang, *NTUm-based optimization of heat or heat pump*
756 *driven liquid desiccant dehumidification systems regenerated by fresh air or return air.*
757 Energy, 2018. **158**: p. 269-280.
- 758 16. Wang, X., et al., *A hybrid dehumidifier model for real-time performance monitoring,*
759 *control and optimization in liquid desiccant dehumidification system.* Applied Energy,
760 2013. **111**: p. 449-455.
- 761 17. Wu, Q., et al., *A regulation strategy of working concentration in the dehumidifier of*
762 *liquid desiccant air conditioner.* Applied Energy, 2017. **202**: p. 648-661.
- 763 18. Zhang, L., H. Wei, and X. Zhang, *Theoretical analysis of heat and mass transfer*
764 *characteristics of a counter-flow packing tower and liquid desiccant dehumidification*
765 *systems based on entransy theory.* Energy, 2017. **141**: p. 661-672.
- 766 19. Kumar, R., et al., *Multi absorber stand alone liquid desiccant air-conditioning systems*
767 *for higher performance.* Solar Energy, 2009. **83**(5): p. 761-772.
- 768 20. Das, R.S. and S. Jain, *Experimental performance of indirect air-liquid membrane*
769 *contactors for liquid desiccant cooling systems.* Energy, 2013. **57**: p. 319-325.
- 770 21. Bai, H., et al., *Influences of the mixed LiCl-CaCl₂ liquid desiccant solution on a*
771 *membrane-based dehumidification system: Parametric analysis and mixing ratio*
772 *selection.* Energy and Buildings, 2019. **183**: p. 592-606.
- 773 22. Xiong, Z.Q., Y.J. Dai, and R.Z. Wang, *Development of a novel two-stage liquid*
774 *desiccant dehumidification system assisted by CaCl₂ solution using exergy analysis*
775 *method.* Applied Energy, 2010. **87**(5): p. 1495-1504.

- 776 23. Luo, Y., et al., *Experimental and theoretical research of a fin-tube type internally-cooled*
777 *liquid desiccant dehumidifier*. Applied Energy, 2014. **133**: p. 127-134.
- 778 24. Luo, Y., et al., *Study on an internally-cooled liquid desiccant dehumidifier with CFD*
779 *model*. Applied Energy, 2017. **194**: p. 399-409.
- 780 25. Ou, X., et al., *Experimental investigations on heat and mass transfer performances of*
781 *a liquid desiccant cooling and dehumidification system*. Applied Energy, 2018. **220**: p.
782 164-175.
- 783 26. Das, R.S. and S. Jain, *Performance characteristics of cross-flow membrane contactors*
784 *for liquid desiccant systems*. Applied Energy, 2015. **141**: p. 1-11.
- 785 27. Ge, G., et al., *Comparison of experimental data and a model for heat and mass transfer*
786 *performance of a liquid-to-air membrane energy exchanger (LAMEE) when used for air*
787 *dehumidification and salt solution regeneration*. International Journal of Heat and Mass
788 Transfer, 2014. **68**: p. 119-131.
- 789 28. Ge, G., et al., *Analytical model based performance evaluation, sizing and coupling flow*
790 *optimization of liquid desiccant run-around membrane energy exchanger systems*.
791 Energy and Buildings, 2013. **62**: p. 248-257.
- 792 29. Moghaddam, D.G., et al., *Small-scale single-panel liquid-to-air membrane energy*
793 *exchanger (LAMEE) test facility development, commissioning and evaluating the*
794 *steady-state performance*. Energy and Buildings, 2013. **66**: p. 424-436.
- 795 30. Ge, G., et al., *Comparison of experimental data and a model for heat and mass transfer*
796 *performance of a liquid-to-air membrane energy exchanger (LAMEE) when used for air*

- 797 *dehumidification and salt solution regeneration*. International Journal of Heat & Mass
798 Transfer, 2014. **68**(1): p. 119-131.
- 799 31. Ghadiri Moghaddam, D., R.W. Besant, and C.J. Simonson, *Solution-side effectiveness*
800 *for a liquid-to-air membrane energy exchanger used as a dehumidifier/regenerator*.
801 Applied Energy, 2014. **113**: p. 872-882.
- 802 32. Ghadiri Moghaddam, D., R.W. Besant, and C.J. Simonson, *A methodology for scaling*
803 *a small-scale energy exchanger performance results to a full-scale energy exchanger*.
804 International Journal of Heat and Mass Transfer, 2015. **82**: p. 555-567.
- 805 33. Namvar, R., et al., *Transient heat and moisture transfer characteristics of a liquid-to-air*
806 *membrane energy exchanger (LAMEE) model verification and extrapolation*.
807 International Journal of Heat and Mass Transfer, 2013. **66**: p. 757-771.
- 808 34. Moghaddam, D.G., R.W. Besant, and C.J. Simonson, *Solution-side effectiveness for a*
809 *liquid-to-air membrane energy exchanger used as a dehumidifier/regenerator*. Applied
810 Energy, 2014. **113**(6): p. 872-882.
- 811 35. Chen, X., et al., *Recent research developments in polymer heat exchangers – A review*.
812 Renewable and Sustainable Energy Reviews, 2016. **60**: p. 1367-1386.
- 813 36. Zhang, L.-Z., et al., *Conjugate heat and mass transfer in a hollow fiber membrane*
814 *module for liquid desiccant air dehumidification: A free surface model approach*.
815 International Journal of Heat and Mass Transfer, 2012. **55**(13–14): p. 3789-3799.
- 816 37. Huang, S.M., et al., *Fluid flow and heat mass transfer in membrane parallel-plates*
817 *channels used for liquid desiccant air dehumidification*. International Journal of Heat &
818 Mass Transfer, 2012. **55**(9-10): p. 2571-2580.

- 819 38. Li, Z.X. and L.Z. Zhang, *Flow maldistribution and performance deteriorations in a*
820 *counter flow hollow fiber membrane module for air humidification/dehumidification.*
821 *Journal of Membrane Science*, 2014. **74**(1): p. 421-430.
- 822 39. Zhang, N., S.-Y. Yin, and L.-Z. Zhang, *Performance study of a heat pump driven and*
823 *hollow fiber membrane-based two-stage liquid desiccant air dehumidification system.*
824 *Applied Energy*, 2016. **179**: p. 727-737.
- 825 40. Zhang, N., S.-Y. Yin, and M. Li, *Model-based optimization for a heat pump driven and*
826 *hollow fiber membrane hybrid two-stage liquid desiccant air dehumidification system.*
827 *Applied Energy*, 2018. **228**: p. 12-20.
- 828 41. Liang, C.-H., L.-Z. Zhang, and L.-X. Pei, *Performance analysis of a direct expansion*
829 *air dehumidification system combined with membrane-based total heat recovery.*
830 *Energy*, 2010. **35**(9): p. 3891-3901.
- 831 42. Chen, X., et al., *Experimental investigations of polymer hollow fibre heat exchangers*
832 *for building heat recovery application.* *Energy and Buildings*, 2016. **125**: p. 99-108.
- 833 43. Riffat, S.B., S.E. James, and C.W. Wong, *Experimental analysis of the absorption and*
834 *desorption rates of HCOOK/H₂O and LiBr/H₂O.* *International Journal of Energy*
835 *Research*, 1998. **22**(12): p. 1099-1103.
- 836 44. Chen, X., et al., *Experimental investigation of a polymer hollow fibre integrated liquid*
837 *desiccant dehumidification system with aqueous potassium formate solution.* *Applied*
838 *Thermal Engineering*, 2018. **142**: p. 632-643.
- 839 45. Karlsson, H.O.E. and G. Trägårdh, *Heat transfer in pervaporation.* *Journal of*
840 *Membrane Science*, 1996. **119**(2): p. 295-306.

- 841 46. Zhang, L.Z., Y. Jiang, and Y.P. Zhang, *Membrane-based humidity pump: performance*
842 *and limitations*. Journal of Membrane Science, 2000. **171**(2): p. 207-216.
- 843 47. Zhang, L.Z., *Heat and mass transfer in a randomly packed hollow fiber membrane*
844 *module: A fractal model approach*. International Journal of Heat & Mass Transfer, 2011.
845 **54**(13): p. 2921-2931.
- 846 48. Zhang, L.Z., *Fabrication of a lithium chloride solution based composite supported liquid*
847 *membrane and its moisture permeation analysis*. Journal of Membrane Science, 2006.
848 **276**(1): p. 91-100.
- 849 49. Incropera, F.P. and D.P. DeWitt, *Fundamentals of heat and mass transfer, 6th Edition*.
850 Wiley, New York, 2006.
- 851 50. Seyed-Ahmadi, M., et al., *Transient behavior of run-around heat and moisture*
852 *exchanger system. Part I: Model formulation and verification*. International Journal of
853 Heat & Mass Transfer, 2009. **52**(25): p. 6000-6011.
- 854 51. Vali, A., et al., *Numerical model and effectiveness correlations for a run-around heat*
855 *recovery system with combined counter and cross flow exchangers*. International
856 Journal of Heat & Mass Transfer, 2009. **52**(25): p. 5827-5840.
- 857 52. Fumo, N. and D.Y. Goswami, *Study of an aqueous lithium chloride desiccant system:*
858 *air dehumidification and desiccant regeneration*. Solar Energy, 2015. **72**(4): p. 351-361.
- 859 53. Melinder, Å., *Thermophysical Properties of Aqueous Solutions Used as Secondary*
860 *Working Fluids Doctoral Thesis By*. Energiteknik, 2007.
- 861 54. Taylor, J.R., *Error Analysis The Study of Uncertainties in Physical Measurements 2nd*
862 *Edition*. Epfl, 1982.

863 55. Zhang, L.Z. and J.L. Niu, *Effectiveness Correlations for Heat and Moisture Transfer*
864 *Processes in an Enthalpy Exchanger With Membrane Cores*. Journal of Heat Transfer,
865 2002. **124**(5): p. 922-929.

866 56. RK;, S. and S. DP, *Fundamental of Heat Exchanger Design*. John Wiley & Sons,
867 Hoboken, NJ, 2003: p. 97-164.

868 57. Zhang, L.Z., *An Analytical Solution to Heat and Mass Transfer in Hollow Fiber*
869 *Membrane Contactors for Liquid Desiccant Air Dehumidification*. Journal of Heat
870 Transfer, 2011. **133**(9): p. 092001.

871

872 **Nomenclature**

A	hollow fiber surface area (m^2)
c_p	specific heat capacity (J/kgK)
Cr^*	heat capacity ratio
d	diameter (m)
d_h	hydrodynamic diameter (m)
h	convective heat transfer coefficient (W/m^2K)
h_{fg}	condensation heat of water (J/kg)
k	mass transfer coefficient (m/s)
L	length of the dehumidifier (m)
M	moisture removal rate (kg/s)
m^*	solution-to-air-mass flow rate ratio
\dot{m}	mass flow rate (kg/s)
m_{sen}	sensible heat capacity ratio
m_{lat}	latent heat capacity ratio
n	number of fibres inside the module
NTU	number of heat transfer units
NTU_m	number of mass transfer units
Nu	Nusselt number
Sh	Sherwood number
Sc	Schmidt number
P_{sol}	equilibrium vapour pressure of desiccant solution (Pa)
P	pressure (Pa)
Pr	Prandtl number
Re	Reynolds number
RH	relative humidity (%)
T	temperature ($^{\circ}C$)
u	velocity (m/s)
X	desiccant solution mass fraction (kg KCOOH/kg solution)

Greek symbols

λ	thermal conductivity (W/mK)
ω	specific humidity of the air (kg moisture/ kg air)
ω_r	air to solution specific humidity ratio
ϕ	packing fraction
μ	dynamic viscosity (Pa •s)
ε	effectiveness
δ	thickness of hollow fiber (m)
ρ	solution density (kg/m ³)
ν	kinematic viscosity (m ² /s)
τ	fractal dimension of the fiber module
ψ	diffusivity (m ² /s)

Subscripts

<i>air</i>	air flow
<i>atm</i>	atmospheric pressure
<i>c</i>	dehumidifier cross section
<i>crit</i>	critical value
<i>b</i>	bulk
<i>desi</i>	desiccant
<i>eq</i>	equivalent
<i>exp</i>	experimental
<i>f</i>	fiber
<i>h</i>	Hydraulic
<i>i</i>	inlet, inside
<i>lat</i>	latent
<i>lim</i>	limiting value
<i>m</i>	mass transfer/hollow fiber
<i>num</i>	numerical
<i>o</i>	outlet, outside
<i>ov</i>	overall
<i>s</i>	surface
<i>sen</i>	sensible
<i>sol</i>	solution flow
<i>tot</i>	total
<i>w</i>	water

873

874

875